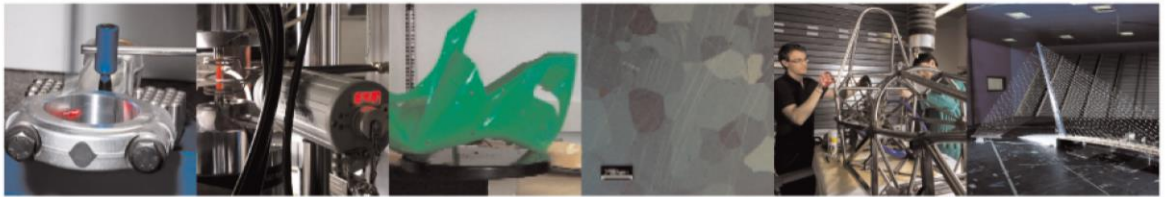




**POLITECNICO**  
MILANO 1863

DIPARTIMENTO DI MECCANICA



## Processability and cracking behaviour of novel high-alloyed tool steels processed by Laser Powder Bed Fusion

Galbusera F., Demir A.G., Platl J., Turk C., Schnitzer R., Previtali B

This is a post-peer-review, pre-copyedit version of an article published in Journal of Materials Processing Technology. The final authenticated version is available online at:  
<http://dx.doi.org/10.1016/j.jmatprotec.2021.117435>

This content is provided under [CC BY-NC-ND 4.0](https://creativecommons.org/licenses/by-nc-nd/4.0/) license



# **Processability and cracking behaviour of novel high-alloyed tool steels processed by Laser Powder Bed Fusion**

Francesco Galbusera<sup>1\*</sup>, francesco.galbusera@polimi.it

Ali Gökhan Demir<sup>1</sup>, aligokhan.demir@polimi.it

Jan Platl<sup>2</sup>, jan.platl@unileoben.ac.at

Christoph Turk<sup>3</sup>, christoph.turk@bohler-edelstahl.at

Ronald Schnitzer<sup>2</sup>, ronald.schnitzer@unileoben.ac.at

Barbara Previtali<sup>1</sup>, barbara.previtali@polimi.it

<sup>1</sup>Department of Mechanical Engineering, Politecnico di Milano, Via La Masa 1, 20156 Milan, Italy

<sup>2</sup>Department of Materials Science, Montanuniversität Leoben, Franz-Josef-Straße 18, 8700 Leoben, Austria

<sup>3</sup>voestalpine Böhler Edelstahl GmbH & Co KG, 8605 Kapfenberg, Austria

\*Corresponding author

# **Processability and cracking behaviour of novel high-alloyed tool steels processed by Laser Powder Bed Fusion**

Francesco Galbusera<sup>1\*</sup>, Ali Gökhan Demir<sup>1</sup>, Jan Platl<sup>2</sup>, Christoph Turk<sup>3</sup>, Ronald Schnitzer<sup>2</sup>, Barbara Previtali<sup>1</sup>

<sup>1</sup>Department of Mechanical Engineering, Politecnico di Milano, Via La Masa 1, I-20156 Milan, Italy

<sup>2</sup>Department of Materials Science, Montanuniversität Leoben, Franz-Josef-Straße 18, A-8700 Leoben Austria

<sup>3</sup>voestalpine Böhler Edelstahl GmbH & Co KG, A-8605 Kapfenberg, Austria

## **Abstract**

Concerning tooling applications, Laser Powder Bed Fusion (LPBF) enables new features such as internal cooling channels that can be implemented in cutting or shaping tools. Thus, higher cutting speeds are feasible thanks to the more efficient cooling that could not be obtained by channels fabricated with conventional methods. However, the alloys exploited for the cutting tools production usually contain high levels of carbon, which makes their LPBF processability challenging due to their high crack-susceptibility. In this work, an approach based on the use of basic physical/empirical indicators has been employed to map the processability of six novel high-alloyed tool steel grades. A large experimental campaign with variable energy densities, single and double passes, as well as different focal points was designed. The results exhibit highly dense but cracked parts. In particular, the LPBF processability deteriorates with increasing carbon content, suggesting that mostly chemistry, rather than process parameters, plays a key role in the determination of the LPBF feasibility. The cooling rate, cooling time between 800°C and 500°C, equivalent carbon content, solidification interval, martensite start temperature and volumetric energy density were employed as indicators to provide a rapid classification of processability. The work demonstrates that the combined use of the indicators can predict the cracking behaviour of carbon-containing tool steels. At a screening level, this approach based on complementary use of physical/empirical tools, may significantly shorten the experimental effort during the design of new compositions, especially when dealing with cracking susceptible alloys like carbon-containing tool steels.

**Keywords:** Laser Powder Bed Fusion, Tool Steels, High Speed Steels, Cracking, Datamining

## List of Symbols

Symbol	Name	Units
$A_{\text{pore,tot}}$	Total area of the pores	$\text{mm}^2$
$A_{\text{tot}}$	Total area of the section	$\text{mm}^2$
$c$	Specific heat	$\text{J}/(\text{kg K})$
CD	Crack density	$\text{mm}/\text{mm}^2$
CEN	Equivalent carbon content	non-dimensional
CR	Cooling rate	$\text{K}/\text{s}$
CR_1	Cooling rate, first pass	$\text{K}/\text{s}$
CR_2	Cooling rate, second pass	$\text{K}/\text{s}$
E	Energy density	$\text{J}/\text{mm}^3$
$E_1$	Energy density – first pass	$\text{J}/\text{mm}^3$
$E_2$	Energy density – second pass	$\text{J}/\text{mm}^3$
$f$	Focal position	mm
$h_d$	Hatch distance	$\mu\text{m}$
$k$	Thermal conductivity	$\text{W}/(\text{K m})$
$L_i$	Crack length	mm
$M_s$	Temperature of martensite start	K
N	Number of passes	non-dimensional
P	Laser power	W
$p_d$	Point distance	$\mu\text{m}$
RD	Relative density	non-dimensional
T	Temperature	K
t	Time	s
$T_0$	Initial temperature	K
$t_{\text{on}}$	Exposure time	$\mu\text{s}$
$z$	Layer thickness	$\mu\text{m}$
$\Delta T$	Solidification interval	K
$\Delta t_{8/5}$	Cooling time between 800°C and 500°C	ms
$\Delta t_{8/5\_1}$	Cooling time, first pass	ms
$\Delta t_{8/5\_2}$	Cooling time, second pass	ms
$\rho$	Density	$\text{kg}/\text{m}^3$

# 1 Introduction

The layer-by-layer deposition nature of the laser powder bed fusion (LPBF) process enables new complex geometries for cutting and shaping tools, which cannot be realized with conventional manufacturing processes. In recent years, the fabrication of tools with LPBF processes has become more and more attractive since the process allows the realization of near-net-shaped tools with internal cooling channels to enhance the thermal control and productivity through higher cutting speeds, or with a lightweight design, to improve vibrations control during cutting operation. Fayazfar et al., (2018) reviewed the LPBF processability of several ferrous alloys. Nevertheless, in the scientific literature, very few works focus on LPBF processability of tool steels (see Table 1). According to Sander et al., (2016) tool steels with high strength and low toughness are susceptible to cracking, which makes the process very challenging. The short interaction times and high cooling rates typical of the LPBF process cause large thermal gradients resulting in fine microstructures with high strength and excessive residual stresses. Moreover, Saewe et al., (2019) stated that the temperature gradients developed during the process induce a preferential grain growth along the building direction, which can cause brittleness and trigger cracking. In addition to this, the combination of high carbon content and high cooling rates lead to the formation of a very fine and brittle martensitic microstructure which means additional residual stresses.

The majority of the scientific publications are focused on the understanding of the typical defects encountered, the analysis and evolution of the microstructure, the application of preheating, as well as other non-conventional strategies to reduce defects and achieve fully dense parts. Amongst the studied materials M2 HSS, AISI H13 HSS, AISI M50, HS 6-5-8-3, FeCrMoVC and FeCrMoVWC stand out. Table 1 gives a summary of the tool steels found in the literature with the main outcome regarding their processability.

Table 1: Chemical compositions of tool steels reported in the literature. Each content in the composition is expressed in wt.%

Ref.	Alloy	Processability	C	Si	Mn	Cr	Mo	V	Co	W	Fe
Buls and Humbeeck, 2014; Liu et al., (2011)	M2 HSS	Severe cracking Crack free with BP <sup>(1)</sup> at 473 K	0.9	0.35	0.38	3.97	4.89	1.82	-	6.15	Bal.
Saewe et al., (2020)	HS6-5-8-3	Severe cracking Crack free with BP at 773 K	1.31	0.5	0.3	4.0	4.7	2.9	8.5	6.4	Bal.
Saewe et al., (2019, 2018)	AISI M50	Severe cracking Crack free with BP at 773 K	0.83	0.2	0.25	4.0	4.3	1.05	-	-	Bal.

Yan et al., (2017)	AISI H13	Lower residual stresses with BP	0.41	1.12	0.41	5.20	1.23	1.10	-	-	Bal.
Beal et al., (2008)	AISI H13	Porosity	0.32-0.42	0.85-1.15	0.4	4.75-5.25	1.25-1.75	0.9-1.1	-	-	Bal.
Mertens et al., (2016)	AISI H13	Cracking Crack free and lower residual stresses with BP at 573 K	0.32-0.4	1.0	-	5.13-5.25	1.33-1.4	1.0	-	-	Bal.
Krell et al., (2018)	AISI H13	Cracking Crack free with BP at 573 K	0.39	1.0	0.3	4.9	1.2	1.0	-	-	Bal.
Narvan et al., (2019)	AISI H13	Cracking Crack free with BP at 573 K	0.39	1.08	0.40	5.27	1.34	0.97	-	-	Bal.
Sander et al., (2016)	Fe85Cr4Mo8V2C1	Crack – free with BP at 773 K	1	-	-	4	8	2	-	-	Bal.
J. Sander et al., (2017)	Fe85Cr4Mo8V1C1	Crack – free with BP at 773 K	1	-	-	4	8	1	-	-	Bal.
J Sander et al., (2017a)	FeCr4Mo1V1W8C1	Crack – free with BP at 773 K	1	-	-	4	1	1	-	8	Bal.
Platl et al., (2020a)	-	Severe cracking Porosity	0.85	0.53	0.36	4.25	2.72	2.01	4.35	2.46	Bal.

<sup>(1)</sup>Baseplate Preheating (BP)

On the one hand, only a few authors studied the LPBF processability of High Speed Steels (HSS). Buls and Humbeeck, (2014) showed that (Liu et al., 2011)(Saewe et al., 2020, 2019, 2018) that extensive cracking, delamination and distortion are present in the built parts. With the aim of investigating M2 HSS LPBF feasibility(Buls and Humbeeck, 2014) Liu et al., (2011) consider the aforementioned defects, the result of the high thermal stresses induced during the process along with the high carbon content of the alloy. Similarly, Saewe et al., (2020) addressed the cause of cracking to the combination of the high carbon content and the rapid solidification of steels, investigating the LPBF feasibility of AISI M50 and H 6-5-8-3. To counterbalance these unwanted defects, especially cracking, preheating of the baseplate is always performed. Buls and Humbeeck, (2014) and Liu et al., (2011) stated that a baseplate preheating up to 473 K was sufficient to obtain crack – free parts of M2 HSS. Also Saewe et al., (2020) obtained crack – free specimens exploiting baseplate preheating up to 773 K for LPBF HS6-5-8-3 and AISI M50. This confirms that the beneficial effect of baseplate preheating comes with the reduction of temperature gradients inside the parts.

On the other hand, several works deal with the LPBF manufacturing feasibility of AISI H13, a versatile Cr-Mo tool steel widely used in hot work tooling applications. Krell et al., (2018) and Mertens et al., (2016) stated that Cr-Mo tool steel exhibits a complex processing behaviour due to the combination of carbon content, rapid

solidification and additional stresses caused by martensite formation, often resulting in cracks and distortion. Narvan et al., (2019) reported a significant reduction of cracks inside the AISI H13 parts whenever baseplate preheating is exploited, usually up to 573 K. Yan et al., (2017) observed a mitigation of residual stresses left in the parts whenever baseplate preheating is applied. Beal et al., (2008) investigated the effect of the scanning strategy on the processability of AISI H13 as an alternative solution for the reduction of thermal stresses, porosity and shrinkage.

Other publications focused on the LPBF processability of Fe85Cr4Mo8V2C1, Fe85Cr4Mo8V1C1 and for FeCr4Mo1V1W8C1, made by J. Sander et al., (2017), demonstrated that high dense and crack-free parts can be obtained using baseplate preheating up to 773 K. Due to the high carbon contents, the microstructure usually comprises of martensite, retained austenite and carbides. Moreover, the high cooling rates of LPBF induce an extraordinarily fine microstructure, usually with elongated grains in the direction of the heat flow (building direction). This is consistent with all the other works, even though the compositions of materials are different. Recently Platl et al., (2020a) studied LPBF of a cold work tool steel with high carbon content and investigated the evolution of defect structure. Extensive cracking along with porosity were observed at different energetic inputs. According to the work of Cunningham et al., (2017), at low energetic conditions, porosity is often generated due to insufficient melting of the powder (lack of fusion mechanism). Oppositely, as observed by Martin et al., (2019), at high energetic conditions, porosity may be formed due to gas entrapment in the melt pool (keyhole mechanism) mostly associated to melt pool instabilities. Concerning the predominant cracking mechanism, a clear correlation between solidification structure and potential stress accumulations, which result from the complex thermal cycle during LPBF, was found.

The major outcomes of the literature point out that LPBF of tool steels remains highly challenging due to the cracking phenomenon, which may be induced by different contributing factors. A large fraction of the published works is based on iterations of different chemical compositions starting from conventional tool steels. Simple analytical and empirical tools would be of great aid to the compositional development of the next generation tool steels. The chemistry of the materials employed in LPBF is usually adopted from alloys processed by the conventional manufacturing processes such as casting. Instead, during the LPBF processes, the rapid cooling and solidification may cause the defects related to the formation of fragile phases as well as high internal stresses. At a material development level, one solution can be to test each new alloy in an iterative

way with large experimental plans. This approach, based on intensive experimental tests, should be aided with analytical tools that reduce the process iterations as well as provide insights to the further steps of the alloy design. The processability of tool steels is indeed one of the current topics in AM that can be tackled by combining computational and experimental approaches as discussed by Smith et al., (2016). For instance (Yan et al., 2018) demonstrated that the use of quick calculation analytical tools can be exploited for establishing the process, material, property relationship especially when large experimental runs are concerned. As discussed by Kouraytem et al., (2020), combining physics and data driven approaches, the results can also be better interpreted along different alloying grades and LPBF machine types providing. To the authors' best knowledge, no previous works have attempted to assess the feasibility of using known rapid analytical and empirical calculations as LPBF processability indicators of new alloys, in particular tool steels.

In this work, the LPBF feasibility of six high-alloyed tool steels grades novel to the LPBF process were studied. In particular, the cracking behaviour was investigated. An experimental campaign with variable energy density, number of passes and focal position was applied to all the material compositions using an industrial LPBF system able to work with small quantities of powder. Among the proposed indicators, cooling rate (K/s), cooling time (s), martensite start temperature (K), solidification intervals (K) and volumetric energy density ( $J/mm^3$ ) were assessed as processability indicators. Crack density was associated to the process parameters as well as the analytical and empirical indicators. The results were also used to interpret the defect formation mechanisms.

## 2 Physical and empirical models

In this section, the physical and empirical models used to map the LPBF feasibility of the alloys under investigation are presented. Each model is limited in terms of its applicability owing to the assumptions employed in their derivation, that might be physical or empirical. Table 2 summarizes the model formulation along with the main defect type they are intended to indicate and the origin (physical or empirical). In particular, the selected indicators are:

- Cooling time between 800°C and 500°C ( $\Delta t_{8/5}$ ) and cooling rate (CR) are conventionally used in welding to predict hardness, toughness and microstructure of a welded joint. Welding parameters should be varied within specific ranges to guarantee the mechanical strength of the joint and prevent



welding defects, such as cracks. Ouden and Hermans, (2009) states that these indicators are estimated using the analytical 3D moving heat source model. Since high cooling speeds may induce internal stresses and the formation of brittle carbon martensite in tool steels, which may result in the formation of cold cracks, these analytical indicators are used to predict the cold cracking susceptibility.

- The equivalent carbon content (CEN) is used to predict the heat affected zone hardenability and again cold cracking susceptibility. Ouden and Hermans, (2009) state that this empirical indicator considers the effect of carbon along with other alloying elements on the risk of brittle phase transformations during cooling. In welding processes, the higher the CEN, the more challenging the welding operation. A threshold value of approximately 0.45 basically indicates good weldability
- The martensite start temperature ( $M_s$ ) determines at which temperature the first martensite transformation occurs. This empirical indicator considers only the effect of alloying elements in the composition of a steel. Depending on the composition, this temperature could be lower than the ambient temperature, suggesting martensite suppression at ambient temperature. Platl et al., (2020b) proposed empirical formulas ( $M_{S0}$ ,  $M_{S1}$ ,  $M_{S2}$  – see Table 2, alloying element contents have to be inserted in wt.%) based on thermodynamic calculations for predicting  $M_s$  of the investigated HSS. However, their investigations were performed on conventionally manufactured HSS and are therefore only of limited applicability for the even higher supersaturated condition that should be present in the as-built state after LPBF.
- Solidification interval ( $\Delta T$ ) describes the temperature range between liquidus and solidus line in a phase diagram. The wider the solidification intervals, the higher the risk of hot cracking. Therefore, the interval estimates (simulated by means of Thermocalc software) could predict the hot cracking susceptibility. For the estimation it was decided to use the Scheil Gulliver model with the back diffusion mode. Compositions of the alloys were set using the available databases TCFE9 (Steels/Fe-Alloys v9.1) and MOBFE4 (Steels/Fe-Alloys Mobility v4.0). It was decided to set the solidification cooling rate at  $10^4$  K/s and to end the simulation at a fraction of liquid phase at 0.05% for a comparison between the different chemical compositions. The calculated cooling rates may differ between the different processing conditions employed in the experimental work. The solidification intervals did

not vary significantly within the experimented range. Hence, a fixed cooling rate was employed. For detailed information about the calculations see the Appendix.

- Energy density (E) is the volumetric energy transmitted by a laser beam with a given power to a material. This physical indicator synthetically comprises the effect of the main LPBF process parameters and can be used to compare different energy input conditions and predict densification during the LPBF process.

A detailed description of each indicator is provided in the Appendix.

Table 2: List of analytical and empirical models used in this work

Name	Ref.	Defect susceptibility	Model type	Formula
Cooling time between 800°C and 500°C	(Ouden and Hermans, 2009)	Cold cracking	Physical	$\Delta t_{8/5}(s) = \frac{P t_{on}}{2\pi k p_d} \left\{ \frac{1}{500 - T_0} - \frac{1}{800 - T_0} \right\}$
Cooling rate	(Ouden and Hermans, 2009)	Cold cracking	Empirical	$CR \left( \frac{K}{s} \right) = - \frac{2\pi k p_d (T - T_0)^2}{P t_{on}}$
Equivalent carbon content	(Yurioka, 2001; Yurioka et al., 1983)	Weldability and cold cracking	Empirical	$CEN = C + A(C) * \left( \frac{Si}{24} + \frac{Mn}{6} + \frac{Cu}{15} + \frac{Ni}{60} + \frac{Cr + Mo + Nb + V}{5} + 5B \right) \text{ wt. \%}$ where $A(C) = 0.75 + 0.25 * \tanh[20 * (C - 0.12)] \text{ wt. \%}$
Martensite start temperature	(Platl et al., 2020b)	Martensite suppression	Empirical	$M_{s0}(K) = 561 - 474 * C - 33 * Mn - 17 * Cr - 17 * Ni - 21 * Mo - 7.5 * Si + 273.15$ $M_{s1}(K) = 550 - 350 * C - 40 * Mn - 35 * V - 20 * Cr - 17 * Ni - 10 * Cu - 10 * Mo - 8 * W + 273.15$ $M_{s2}(K) = 0.495 * M_{s1}(^{\circ}C) + 0.00095 * M_{s1}(^{\circ}C) + 313.15$
Solidification interval	(Kozeschnik et al., 2007; Schaffnit et al., 2015)	Hot cracking	Physical with Thermocalc	$\Delta T(K)$
Energy density	(Carluccio et al., 2019)	Densification, LPBF	Physical	$E \left( \frac{J}{mm^3} \right) = \frac{P t_{on}}{p_d h_d z}$

According to the formulas, some of the indicators are only composition dependent, such as the CEN and the  $M_s$ , whereas others also depend on the process parameters. The indicators that are linked to the process parameters, namely  $\Delta t_{8/5}$ , CR and E were calculated separately for each laser pass. These models were adapted to the pulsed wave (PW) laser emission mode employed in the experimental study. It must be noticed that none of these indicators was developed for LPBF processes, where typical cooling rates are one-two times order of

magnitude faster than cooling rates experienced in traditional welding processes (Saewe et al., 2019; J. Sander et al., 2017), where these indicators are usually used (Poorhaydari et al., 2005).

### **3 Materials and methods**

#### **3.1 Laser powder bed fusion system**

An industrial LPBF system, (Renishaw AM250, Stone, UK) was used throughout this work. The system is equipped with an Yb:glass single mode fiber laser source (R4, SPI, Southampton, UK), operating with a wavelength of 1070 nm, a maximum power of 200 W and a beam diameter in the focus position of 70  $\mu\text{m}$ . The laser source operates with pulsed wave (PW) emission by power modulation to achieve  $\mu\text{s}$ -long pulses. The laser emits with a determined power (P) level and exposure time ( $t_{\text{on}}$ ) with a constant scanner movement emitting pulses with the determined point distance ( $p_d$ ). Once the line is scanned, the laser jumps to and adjacent scan vector spaced with a hatch distance ( $h_d$ ). After the completion of the layer, the powder bed is lowered with the determined layer thickness (z). The laser focal position (f) can be also adjusted with respect to the powder bed. The system operates in a controlled atmosphere. Before building, the chamber is filled with Ar with 15 mbar overpressure so that the oxygen content is maintained below 1000 ppm. The LPBF system was equipped with a reduced build volume (RBV) platform which limits the available build volume to  $78 \times 78 \times 50 \text{ mm}^3$  for testing new alloys using small quantities of powder.

#### **3.2 Materials**

In the present investigation six novel high-alloyed tool steels were processed. The feedstocks were produced through powder atomization (voestalpine Böhler Edelstahl GmbH & Co KG, Kapfenberg, Austria). The designation and the nominal chemical compositions of the alloys are reported in Table 3 whilst the scanning electron microscope (SEM, Tescan Clara device with an acceleration voltage of 15 kV and a working distance of 15 mm) images of the powders are shown in Figure 1 in secondary electron detection mode. Particle size measurements revealed that powder granulometries are comprised between 15 and 45  $\mu\text{m}$  and that particles have a spherical shape with few satellites, without internal porosity and featured by a dendritic solidification structure. The declared thermophysical properties ( $\rho$ : density, c: specific heat, k: heat conductivity) of the alloys under investigation are summarized in Table 4.

Table 3: Designation and nominal chemical compositions of the tool steels alloys in wt%. Letters denote the alloy type.

Alloy	Designation	C	Si	Mn	P	S	Cr	Mo	Ni	V	W	Cu	Co	N	O	Fe
A	Fe25Co15Mo	0.01	-	-	-	-	-	15	-	-	-	-	25	-	-	Bal.
B	HS3-3-2-5	0.85	0.53	0.36	0.019	0.011	4.25	2.72	0.19	2.01	2.46	0.1	4.35	0.04	0.004	Bal.
C	HS6-5-3-8	1.28	0.6	0.29	0.019	0.016	4.04	4.91	0.21	2.97	6.12	0.12	8.19	0.047	0.005	Bal.
D	HS6-5-4	1.31	0.58	0.29	0.020	0.013	4.07	4.94	0.2	3	6.13	0.13	0.24	0.054	0.003	Bal.
E	HS6-5-3C	1.34	0.56	0.29	0.023	0.017	3.99	4.92	0.16	3.95	5.43	0.11	0.28	0.061	0.008	Bal.
F	HS10-2-5-8	1.62	0.31	0.25	0.021	0.013	4.86	1.87	0.26	4.7	10.23	0.12	7.82	0.058	0.004	Bal.

Table 4: Thermophysical properties (density, specific heat and heat conductivity) of the alloys under investigation at room temperature declared by the powder provider.

Alloy	Density, $\rho$ (kg/m <sup>3</sup> )	Specific heat, $c$ (J/kg K)	Heat conductivity, $k$ (J/K m s)
A	8315	420	24
B	7850	450	22.5
C	8050	420	22
D	8000	420	24
E	7900	440	20
F	8100	420	17

Danninger et al., (2013) describes alloy A as a carbon-free tool steel whose composition is suitable for cutting applications. On the other hand, Platl et al., (2020a) investigated LPBF processability of alloy B, which is a cold work tool steel; C-F are HSS with elevated carbon contents. The alloys were denoted with letters, in ascending order of the carbon content. Throughout the experimental activity, conventionally hot isostatic pressed and soft annealed baseplates with a similar chemical composition of the investigated alloys were used apart for the alloy A, for which a conventional low carbon steel plate was used.

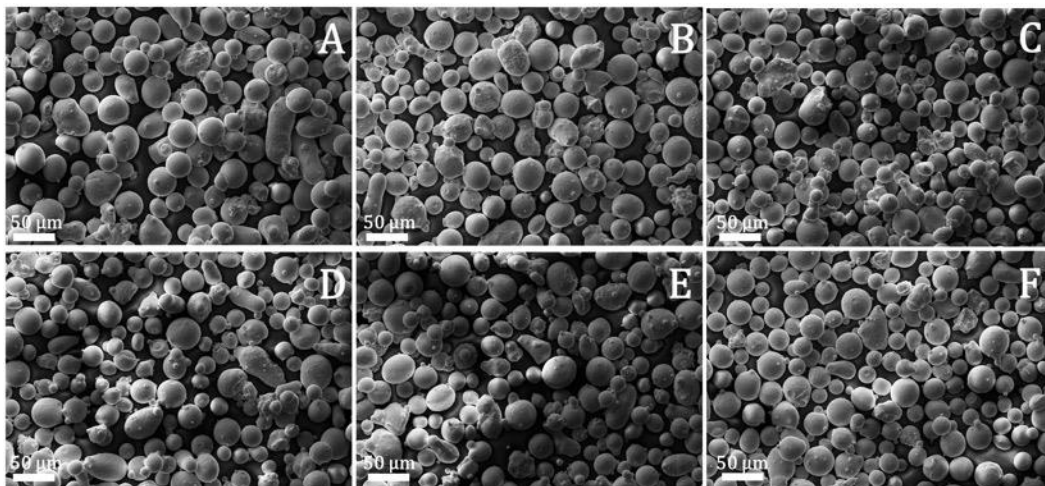


Figure 1: SEM images showing the spherical morphology of the used powders. Letters denote the alloy type.

### 3.3 Experimental campaign

To investigate the LPBF feasibility of the tool steels, an experimental campaign was designed involving the use of multiple passes and defocusing as potential strategies to decrease the high thermal gradients and thus cracking tendency. Small cubes with dimensions of  $5 \times 5 \times 5 \text{ mm}^3$  were built with constant laser power and layer thickness (200 W and 40  $\mu\text{m}$ , respectively). It was decided to vary the focal position ( $f$ ), the number of passes ( $N$ ) and the energy density ( $E$ ), as shown in Table 5. The multiple scan strategy was employed as a means of crack mitigation. Between the multiple passes, the scan direction was varied by  $90^\circ$  as previously employed in the work of Demir and Previtali, (2017) with multiple pass strategies. The energy density was divided into the number of passes equally. Hence, with a single pass, the whole energy density was released, while with two passes at each pass half of the energy density was released. Demir et al., (2017) estimated the beam diameter in the defocused condition ( $f=3 \text{ mm}$ ) as 290  $\mu\text{m}$ . The use of a second pass can be exploited to fill the previously generated crack by a remelting operation. The use of a defocused beam can be beneficial to avoid high intensity around the beam centre, which may generate a larger temperature gradient along the melt pool. The experimental plan was applied to each alloy, resultantly “Material” was treated as a block factor. For each experimental condition, the values of process parameters ( $p_d$ ,  $h_d$ ,  $t_{on}$ ) were calculated starting from preliminary experiments.

Table 5: Fixed and varied parameters used in the experimental campaign

<b>Fixed parameters</b>	
Laser power, P, (W)	200
Layer thickness, z, ( $\mu\text{m}$ )	40
<b>Varied parameters</b>	
Focal position, f, (mm)	0, 3
Number of passes, N, (-)	1, 2
Energy density, E, ( $\text{J}/\text{mm}^3$ )	50, 60, 70, 80, 90, 100, 110
Material	A, B, C, D, E, F

The samples were detached from the baseplates and then embedded into resin and polished following conventional metallographic analysis procedures. Micrographs of metallographic cross sections along the build direction were taken with an optical microscope (Mitutoyo, QV ELF202, Kanagawa, Japan). The images were used to measure the relative density (RD) and crack density (CD), measured with an image processing software (ImageJ, U.S. National Institutes of Health, Bethesda, Maryland, USA). Crack and relative density must be

considered as indicators of the defect distribution, cracking and porosity, respectively. As shown in Figure 2, after applying the adequate filtering procedure, bulk regions will appear black and pores white.

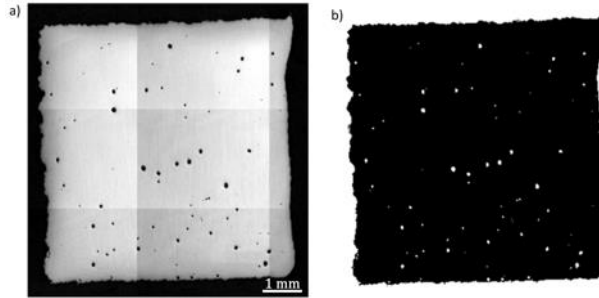


Figure 2: a) Metallographic cross section; b) Black and white conversion of the cross section.

RD was calculated through the processed images as the ratio expressed in the following equation proposed by Carluccio et al., (2019):

$$RD (\%) = \left(1 - \frac{A_{\text{pore,tot}}}{A_{\text{tot}}}\right) * 100\%, \quad 1$$

where  $A_{\text{pore,tot}}$  is the total area of the pores, which corresponds to the white regions within the cross section after conversion (Figure 2b), and  $A_{\text{tot}}$ , which is the total area of the section (bulk and pores).  $A_{\text{tot}}$  is delimited by a perimeter traced within the outer borders of the samples. Whenever a cracks develops inside the cross section, the perimeter circumscribes the crack itself so to avoid possible fake measurements induced by inner cracks. Crack density (expressed in  $\text{mm}/\text{mm}^2$ ) was calculated with the following equation proposed by Zou et al., (2018):

$$CD \left(\frac{\text{mm}}{\text{mm}^2}\right) = \frac{\sum_i L_i}{A_{\text{tot}}} \quad 2$$

where  $L_i$  is the length of an individual crack and  $A_{\text{tot}}$  is the total area of the cross section. ImageJ automatically returns the length of traced segments. Therefore, to evaluate the crack extension, each crack length was measured following the centreline of the crack route within a section, as shown in Figure 3.

Indeed, the correct reconstruction of the defects in LPBF parts is a complex issue. The employed measurement strategy with the optical microscopy images were found to be the best compromise (Spierings et al., 2011). The use of the Archimedes method for porosity would have generated issues due to possible gas entrapment in the cracks and corrosion during the measurement process if water is used. X-ray tomography is a possible route, which would require high resolution and dedicated image processing algorithms to distinguish the

different defect types, which has not been the main objective of this work. Analysis of variance (ANOVA) was applied to the crack density as the main investigated output. A statistical significance level of  $\alpha=5\%$  was employed in the analysis.

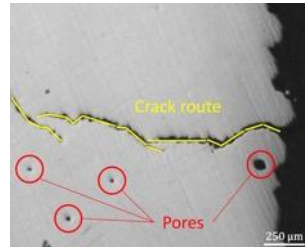


Figure 3: Detail of crack extension measurements. Yellow segments denote the crack route and red circles denote pores.

SEM images (SEM, EVO-50, Carl Zeiss, Oberkochen, Germany) and Vickers microhardness were measured on selected samples with 2 kgf applied load (VMHT 30A, Leica, Wetzlar, Germany).

Cooling rate CR and times  $\Delta t_{8/5}$  were calculated for each pass employing the process parameters. Thermocalc software (Stockholm, Sweden) was used to estimate solidification intervals of the alloys under investigation. Compositions of the alloys were set using the available databases TCFE9 (Steels/Fe-Alloys v9.1) and MOBFE4 (Steels/Fe-Alloys Mobility v4.0). Cooling rate, time, and solidification interval calculations were not experimentally validated, but were used for a comparison between the different alloy types. Such calculations have been previously employed in literature for assessing the processability of the LPBF materials (Saewe et al., (2019)). Validation of these parameters would have required high speed imaging, thermography or X-ray tomography, which are not within the main objectives of this work.

The calculated indicators were used to verify any relation to the the crack density data in order to grasp a better understanding of the processability.

## 4 Results

### 4.1 Macroscopic appearance

Figure 4 shows the macro view of the produced samples. It can be noted that the processability of the materials varies greatly, in particular the processability decreases with increasing carbon content. It can be stated that:

- Alloys A and B appear as the most processable alloys because no macroscopic defects are visible.

- With increasing carbon content, alloys C, D and E suffer from delamination from the baseplate, severe cracking starting from the edges and excessive deformation.
- Alloy F is not processable, irrespective of the experimental conditions.

For alloy C, D, and E, the build jobs were interrupted after 80 – 90 layers (about 3 mm) because most of the samples showed protruding edges above the powder bed. Concerning alloy F, the build job was interrupted after 10 – 20 layers due to the severe cracking and delamination that caused spontaneous detachment of the build job from the base plate. Since for alloy F no samples were built, no further analysis was conducted.

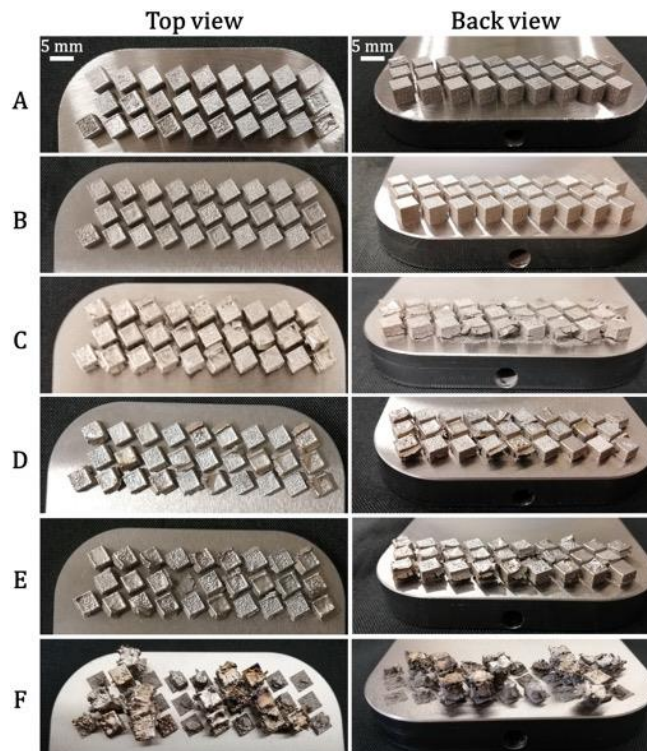


Figure 4: Top and back view of the building platforms for each alloy. Letters denote the alloy type.

## 4.2 Relative density and crack density

Figure 5 shows the comparison between the worst and best case in terms of relative density for each alloy. Lack of fusion pores at low energy density and keyhole porosities at high energy density conditions were observed, consistently with the work of Narvan et al., (2019). The cracking behaviour appears almost independent from the densification of the materials and is always present with variable severity.




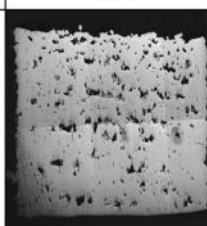
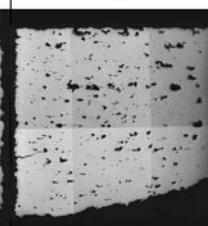
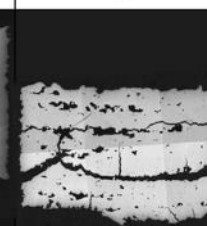
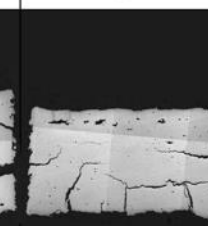
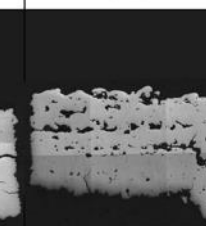


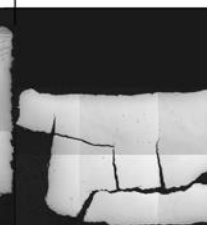
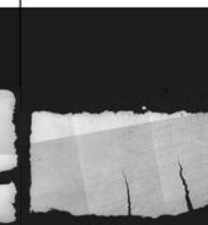
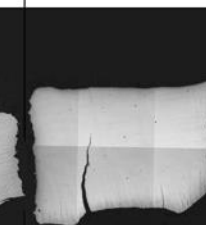
	A	B	C	D	E	F
						
<b>Worst</b>						NA
	E=60 J/mm <sup>3</sup> ; f=0 mm; N=2	E=60 J/mm <sup>3</sup> ; f=3 mm; N=2	E=60 J/mm <sup>3</sup> ; f=3 mm; N=2	E=60 J/mm <sup>3</sup> ; f=3 mm; N=2	E=60 J/mm <sup>3</sup> ; f=3 mm; N=2	-
<b>Best</b>						NA
	E=80 J/mm <sup>3</sup> ; f=0 mm; N=1	E=60 J/mm <sup>3</sup> ; f=0 mm; N=1	E=90 J/mm <sup>3</sup> ; f=0 mm; N=2	E=60 J/mm <sup>3</sup> ; f=0 mm; N=1	E=110 J/mm <sup>3</sup> ; f=3 mm; N=2	-

Figure 5: Metallographic cross sections comparison between the worst and best cases in terms of relative density for each alloy. “BD” stands for Build Direction while letters denote the alloy type.

Figure 6 shows the relative density (RD) of the experimented conditions. It is found that parts with RD > 99% could be produced for alloys A to E. The results depict that adequate densification could be achieved with the correct energy density with a single or double pass strategy employing focused or defocused beams.

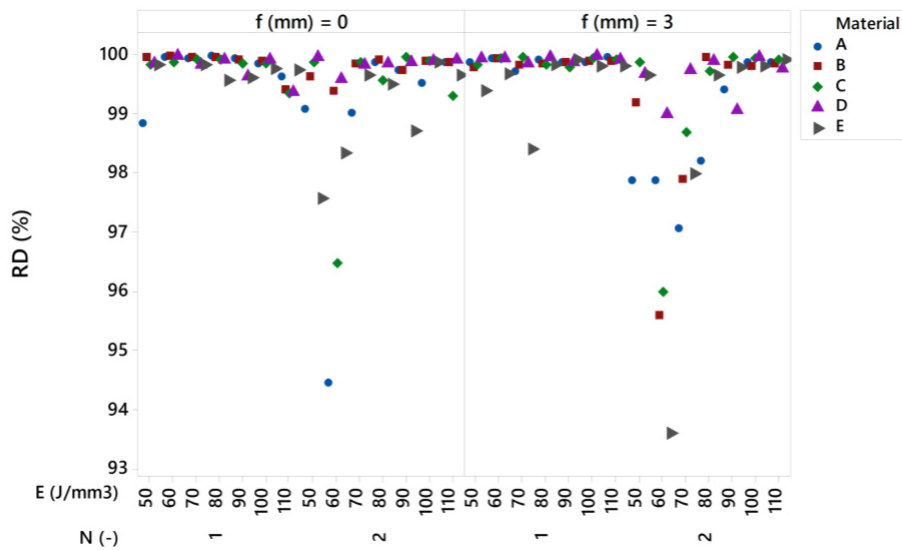


Figure 6: Relative density in dependence of the process parameters for each processed alloy.

In Figure 7 the comparison between the worst and best case in terms of crack density for each alloy is provided. The crack morphology is different between alloy A (carbon-free) and the carbon-containing steels. For alloy

A, cracks propagate perpendicularly to the building direction whereas for the other carbon steels, cracks tend to generate a coherent network inside the section. Crack propagation could either follow the building direction or propagate perpendicularly to the building direction. It can be seen that with the alloys C, D, and E the crack formation was intense in all the experimented conditions, implying that the process parameters were not sufficient to eliminate this defect. In the case of alloy F, no sound specimen was obtained within the large experimental space, indicating that the material is overall unsuitable for the process due to its chemical composition. On the other hand, the effectiveness of the parameters to reduce the intensity of the defect requires a more detailed analysis on the crack density.

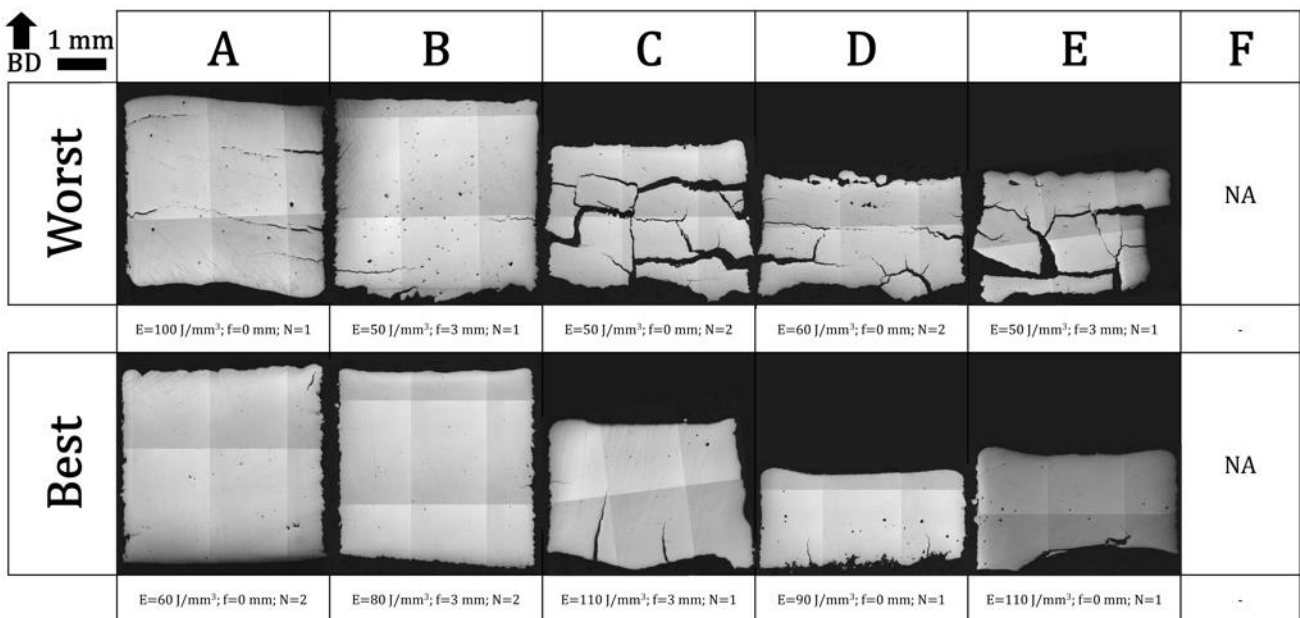


Figure 7: Metallographic cross sections comparison between the worst and best cases in terms of crack density for each alloy. “BD” stands for Build Direction while letters denote the alloy type.

Figure 8 shows the individual value plot of crack density (CD), which results as a function of the experimental conditions. It can be seen that CD can reach extreme severity up to 2 mm/mm<sup>2</sup>. The influence of the alloy type appears to be strongest amongst the analysed factors, where a general reduction of CD can be observed with increasing energy density.

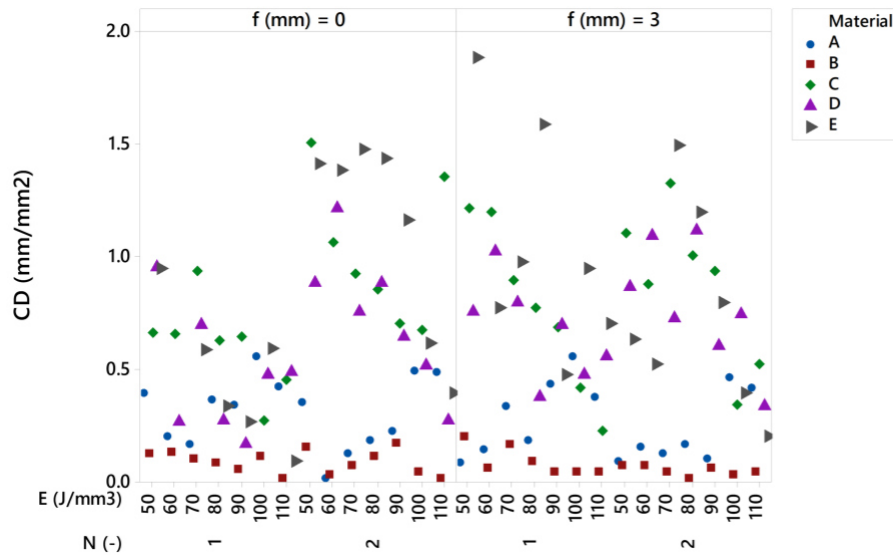


Figure 8: Crack density as a function of the process parameters for each processed alloy.

For a better visualization of the main effects and second order interactions, the plots are employed as shown in Figure 9. In addition, material shows the largest influence on the crack density, while N and f appear to be less influential. In Figure 9b, the interaction plot of crack density is provided. In each box of the plot, CD data is displayed as a function two parameters together, allowing to visualize possible interactions between them. Essentially one parameter is provided on a continuous variable on the y-axis and the second parameter provided in different lines. The interaction plot provides a visual representation of the change in the response when two parameters are changed together. Parallel lines are referable to missing interaction and crossing line to possible interaction. Although Material is the block factor in the analysis, its possible interactions are checked via the interaction plot. It is noted that alloy A behaves differently than the other alloys, where an increase in the energy density increased the crack density. For the rest of the alloys the interaction plot denotes a reduction of the cracks with the increase of the energy density overall. These observations indicate the influence of the process parameters on the cracking intensity and moreover an important interaction between the material chemical composition and the energy input requirements.

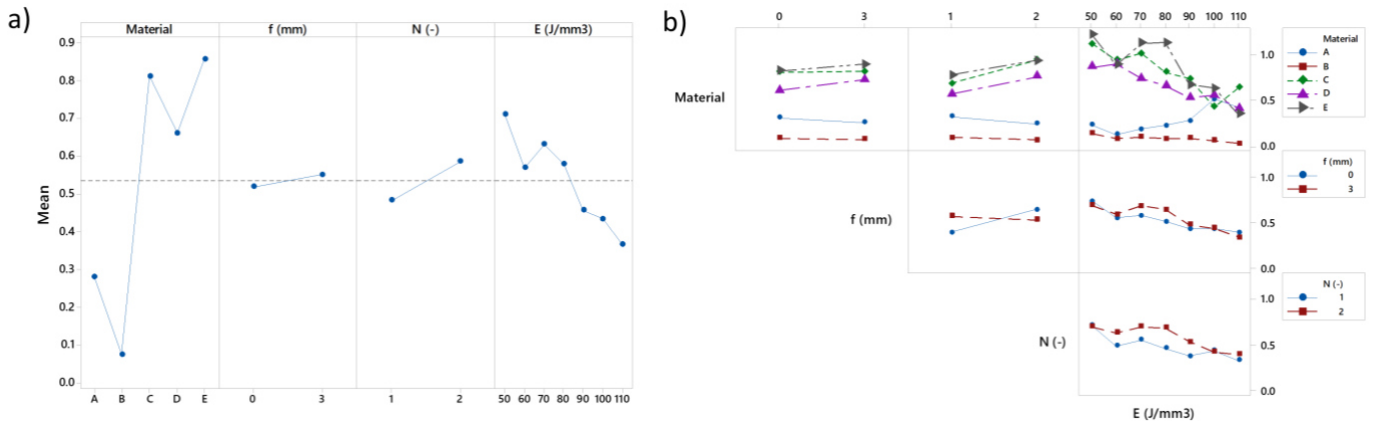


Figure 9: a) Main effects plot of CD data; b) Interaction plot of CD data.

Accordingly, in the analysis of variance (ANOVA) the main effects of all factors and the interactions between f, N, and E were assessed and the results are listed in Table 6. The model comprises Material, f, N and E and the interactions up to the 3<sup>rd</sup> order between f, N and E. The model has an  $R^2_{adj}$  value at 59.94%, which may signal unexplained variability within the model. This can be attributed to the possible interactions with the blocked factor, Material, which could not be evaluated in the statistical analysis. As all the statistical hypotheses were verified, further interpretations were found to be feasible on the significance of the parameters. Separate ANOVA models on each material could have been resulted in a higher  $R^2_{adj}$  value, while an overall comparison between the alloy types would have not been possible. The results show that Material, E, N and the f\*N interaction were significant. Material appears to be the most influential parameter with the highest F-value as also observed in the main effects plot. The effect of Material is predictable from the macro view of the samples shown in Figure 4. The steel grades suffer from different cracking severity with an apparent increase with the increase of the carbon content. The second strongest parameter was found to be E as denoted by its F-value. Overall, a higher volumetric energy density appears to be beneficial for the crack density reduction. Concerning the interaction f\*N, the combination of a focused beam and a single pass appears advantageous for the crack density reduction. However, the effect of this interaction, along with N, is one order of magnitude lower than the effect of Material and E. It can be concluded that the processing strategies adopted for cracking mitigation have a poor effectiveness. Overall the statistical analysis confirms the influence of the processing parameters on the crack formation, while the material chemical composition remains to be most important one.

Table 6: Analysis of variance on crack density and model summary

Source	DF	Adj SS	Adj MS	F-Value	P-Value
--------	----	--------	--------	---------	---------

Material	4	12.9969	3.24923	40.54	<b>0.000</b>
f (mm)	1	0.0311	0.03106	0.39	0.535
N (-)	1	0.3443	0.34430	4.30	<b>0.041</b>
E (J/mm <sup>3</sup> )	6	1.7679	0.29465	3.68	<b>0.002</b>
f (mm)*N (-)	1	0.6985	0.69854	8.72	<b>0.004</b>
f (mm)*E (J/ mm <sup>3</sup> )	6	0.1549	0.02582	0.32	0.924
N (-)*E (J/ mm <sup>3</sup> )	6	0.2445	0.04075	0.51	0.801
f (mm)*N (-)*E (J/ mm <sup>3</sup> )	6	0.1827	0.03045	0.38	0.890
Error	107	8.5764	0.08015		
Total	138	25.1075			

---

#### Model Summary

---

S	R <sup>2</sup>	R <sup>2</sup> <sub>adj</sub>	R <sup>2</sup> <sub>pred</sub>
0.283113	65.84%	55.94%	42.43%

---

### 4.3 Effect of $\Delta T$ , CEN and $M_s$

The Thermocalc simulations of solidification intervals are reported in Figure 10. The effect of rapid solidification on the segregation of alloying elements can be observed comparing the Equilibrium (EQ) model with the Scheil Gulliver Simulation (SGS) and the SGS with Back Diffusion (SGS-BF) curves. All the different solutions are provided for the sake of completeness, while the Scheil Gulliver with Back Diffusion mode (SGS-BF) is the best model to estimate the solidification interval is found to be the most suited one for simulating the conditions present in LPBF. Only at the beginning of the solidification, there is no difference in the models used, but once the solidification has started, the SGS and the SGS-BF start to diverge, amplifying the intervals. Moreover, it can be observed the effect of carbon back diffusion looking at the SGS and SGS-BF curves. Indeed, the partial redistribution of carbon, which is a fast diffusing element, reduces the solidification intervals pushing the solidification closer to the equilibrium curve. During LPBF processing, due to excessive cooling rates, equilibrium conditions during solidification cannot be sustained. Therefore, wider solidification intervals, epitaxial grain growth towards the build direction and a dendritic microstructure are expected.

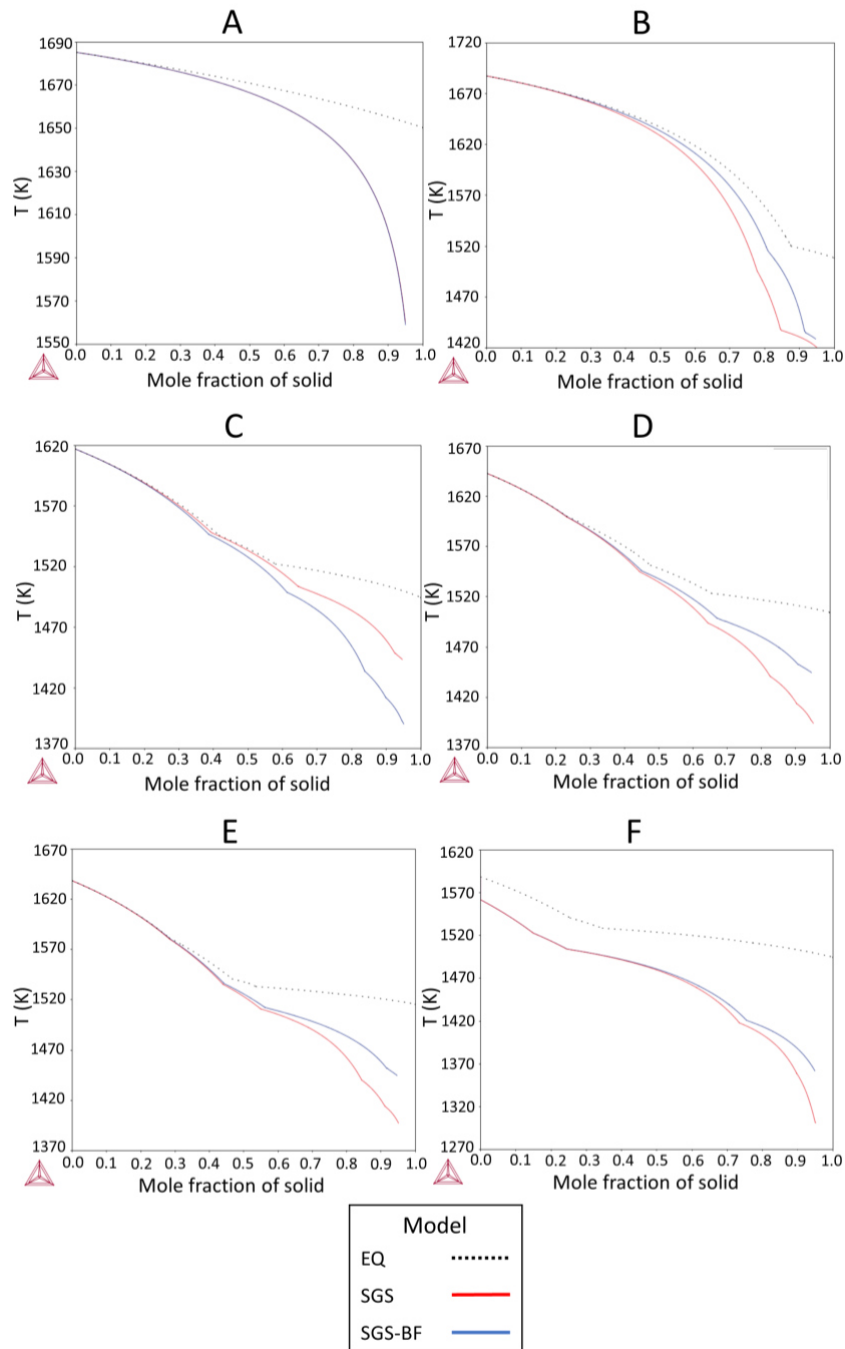


Figure 10: Solidification simulations expressed in T (K) vs Mole fraction of solid diagrams, for all six investigated alloys. Dotted, red and blue lines denote the solidification simulation according to the equilibrium model (EQ), Scheil Gulliver model (SG) and Scheil Gulliver model with back diffusion of carbon (SGS-BF).

In Figure 11 a boxplot of the solidification intervals, estimated with Thermocalc software databases namely TCFE9-Steels/Fe-Alloys v9.1 and MOBFE4-Steels/Fe-Alloys Mobility v4.0 (Thermocalc, 2021) according to the equilibrium model (EQ) and the Scheil Gulliver model with back diffusion (SGS-BF), are depicted. The most important outcome is that, regardless of the carbon back diffusion considered in the model, broad solidifications intervals increase the danger of hot cracking. For alloy A, the observed increase of amplitude is

mainly attributable to the LPBF rapid solidification (high CR). Moreover, the plots imply that moving away from equilibrium conditions towards a more rapid solidification process, the  $\Delta T$  of solidification can be further extended. Hence, the tested alloys can be less problematic for slower cooling processes such as gravity casting, while for processes involving very rapid cooling cycles, they can be more prone to cracking. For further analysis the  $\Delta T$  values calculated via the and Scheil Gulliver model with back diffusion was considered.

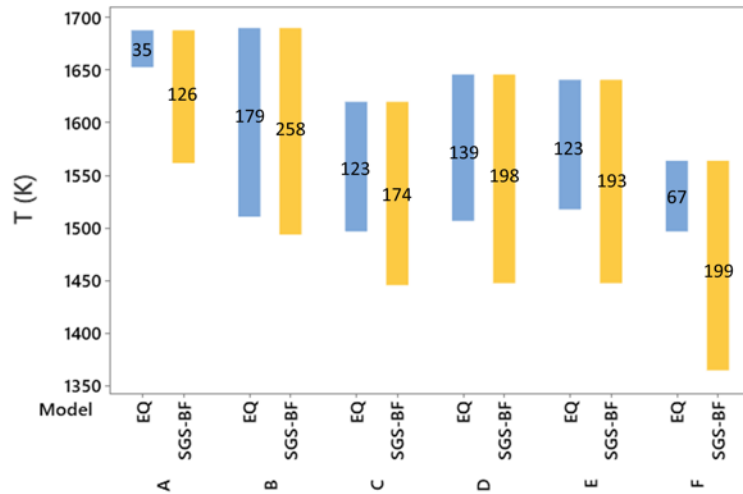


Figure 11: Thermocalc estimations of solidification intervals according to equilibrium solidification model (EQ) and Scheil Gulliver model with back diffusion (SGS-BF).

In Figure 12 crack density data of all the experimental conditions are displayed as a function of CEN,  $M_s$  and  $\Delta T$ , as an attempt to verify the overall processability with these single parameters. The different data dispersions of the different alloy types are related to the influence of the varying process parameters. In Figure 12a and Figure 12b, the alloy A is not presented as it does not contain any carbon.

As seen in Figure 12a, each of the carbon-containing tool steels has a CEN higher than the threshold of good welding, which is approximately 0.45 wt.% according to Ouden and Hermans, (2009), implying poor weldability and high risk of cold cracking. Moreover, CD data dispersion increases with the CEN, or equivalently with the carbon content of the tool steels. This suggests the existence of a carbon content critical threshold in the composition, at least from the technological point of view, above which the LPBF processability is drastically deteriorated. Indeed, alloy F is featured by the highest carbon content and the lowest processability among the processed alloys.

The same CD data are displayed in Figure 12b, but highlighting the effect of  $M_s$ . It can be noticed that a higher carbon content yields in lower  $M_s$ , which ranges between 330 K for alloy B and 250 K for the other ones. This

holds also for alloy F for which no CD data were available. The martensite start temperatures depicted in Figure 12b were calculated using the  $M_{s2}$  formula (see Table 2) because, according to the work of Platl et al., (2020b), it should be better suited to estimate  $M_s$  of HSS at high austenitizing temperatures at which carbides may be dissolved (high supersaturation conditions). Close results can be obtained using the other formulas  $M_{s0}$  and  $M_{s1}$ . The calculated values are very low for the martensite formation in conventional steel processing and suggest martensite suppression in the microstructure should occur apart from the alloy B, for which martensite formation is predicted at almost 330 K. Despite the numerical indicators, the crack density values appear to be much larger with the lower  $M_s$  values, suggesting that the indicator is not sufficient to describe the crack susceptibility. As a matter of fact, the  $M_s$  estimations are based on empirical formulas often used in the heat treatments design of specific steels composition. Nor the chemical composition of the tool steels, neither the LPBF thermodynamics resemble the assumptions needed for the  $M_s$  estimation, which limits the applicability of the indicator.

In Figure 12c, CD data are displayed as a function of  $\Delta T$  estimated by means of Thermocalc software using the Scheil Gulliver Simulation with Back Diffusion (SGS-BF). First, it can be noticed that owing to the Scheil Gulliver model assumptions, the segregation of alloying elements, especially carbon, and the LPBF cooling rates, solidification intervals are broad. Secondly, alloy B shows the highest  $\Delta T$  among the carbon-containing tool steels, although it has the lowest carbon content and CEN. Owing to the complexity of chemical compositions and the phase transformations occurring during solidification, it is not easy to understand the mechanism responsible for this behaviour, nonetheless B is the least susceptible alloy to cracking. Overall, the  $\Delta T$  appears to be insufficient to describe the cracking phenomenon. A higher  $\Delta T$  can be attribute to a higher probability of hot cracking formation. On the other hand, all the estimated values are large (126-258°C). For comparison the  $\Delta T$  of AISI 316 as a material with well-known processability was calculated following the same approach as 79°C. It can be seen that the studied alloys are characterized by a much higher interval increasing their susceptibility to hot cracking, while it can be expected that other factors can influence its extent and help suppress when combined. Hence, cooling conditions and fracture images were analysed together with these indicators.



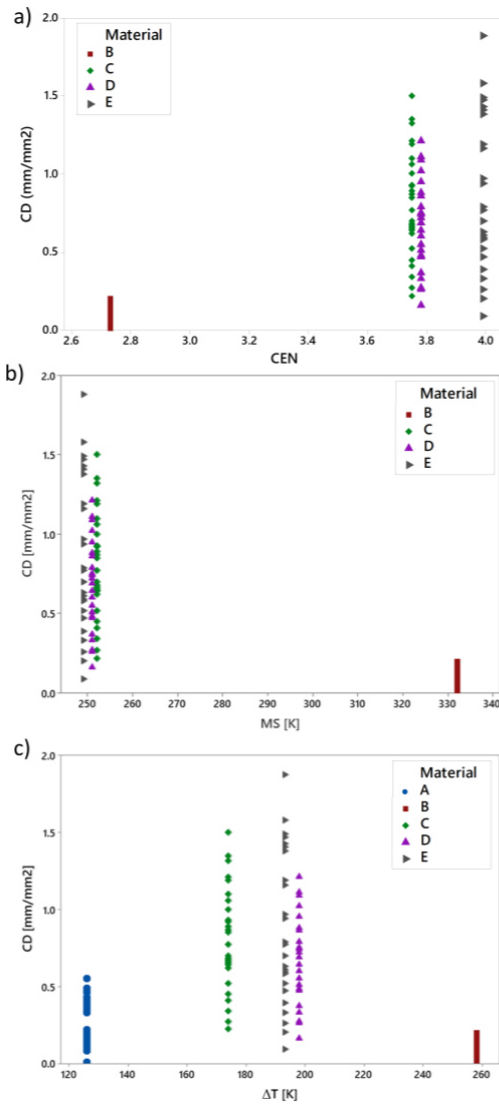


Figure 12: Crack density as a function of a) carbon equivalent content; b) martensite start temperature; and c) solidification interval.

#### 4.4 Effect of CR and $\Delta t_{8/5}$

In Figure 13a and Figure 13b, crack density data are displayed as a function of  $\Delta t_{8/5\_1}$  and CR\_1. Similar results can be obtained when crack density data are plotted in dependence of  $\Delta t_{8/5\_2}$  and CR\_2, whenever the second pass is involved. It should be noted that the cooling times are in the order of a few ms, while the cooling rates are found to exceed  $10^6$  K/s. The influence of the physical properties with respect to the cooling rates under the same processing parameters are shown to be similar for the tested ferrous alloys. This has been confirmed also by the calculations of the cooling rate shown in Figure 13b as the intervals remain similar. The calculations are coherent with the well-known rapid solidification behaviour of the LPBF process mentioned

in the works of Saewe et al., (2019) and J. Sander et al., (2017). The plots are accompanied with dashed lines to depict an overall. While a regression analysis was not sought for these parameters, the dashed lines allow to visualize how different materials follow different trends with the cooling time and rate.

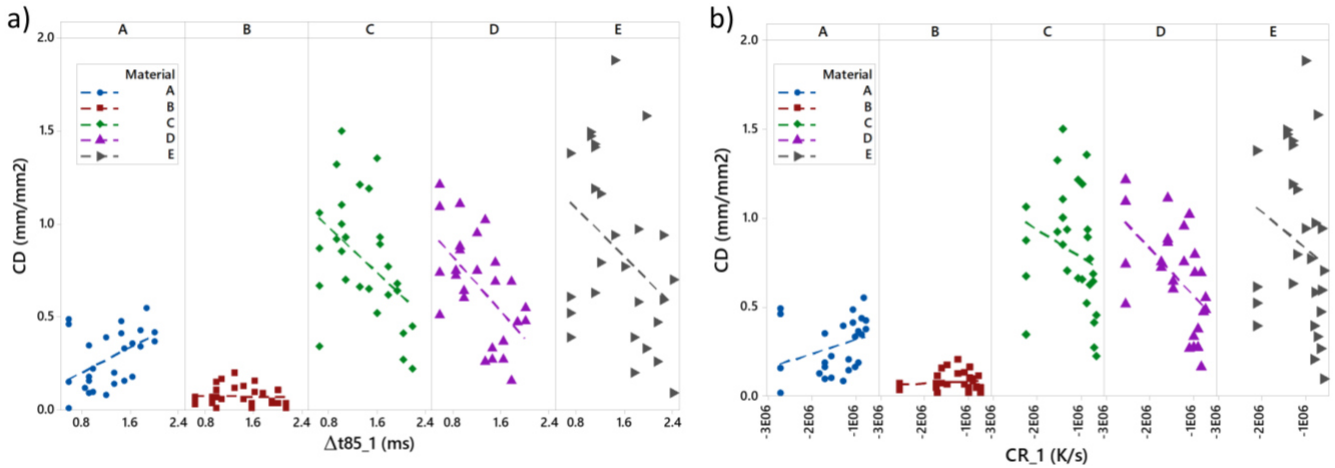


Figure 13: Crack density as a function of a) cooling time and b) cooling rate for the processed alloys. Dashed lines only indicate trends.

From Figure 13a some overall trends can be observed. For alloy A, CD increases with  $\Delta t_{8/5}$ , while for alloy B no significant trend is visible. For alloys C, D and E, CD decreases with  $\Delta t_{8/5}$ . Same considerations hold considering the CR in Figure 13b. The indications that come from these graphs support the idea of cold cracking for the carbon steels, as suggested by CEN indicator. Higher cooling times respectively lower cooling rates are desirable for crack mitigation owing to a reduction of residual stresses, especially for high carbon contents. However, the mechanism of crack formation may be completely different to the mechanism of crack propagation. These trends may provide useful information on the crack propagation mechanism but not the origin of the cracks themselves. In other words, there is the possibility that cracks nucleate following one mechanism, for example hot cracking during solidification, as suggested from the high solidification interval, but propagate due to residual stresses after further cooling, typical of the cold cracking mechanism. On the other hand, crack formation mechanism of alloy A appears to be completely different from the other alloys with respect to the thermal history during the LPBF process. The presence of different cracking mechanisms (solidification and residual stress cracking) has been investigated in the recent work of Wu et al., (2021) dealing with LPBF of AISI H13. The authors stated that these defects are mostly affected by the material composition rather than process parameters.

#### 4.5 Crack surface fractography and phenomenological interpretations

Representative crack fractographs are shown in Figure 14 for the investigated steels. The cracks were formed during the LPBF process and were further opened by means of a hammer and chisel manually. The initial crack zone formed directly by the LPBF process was analysed under SEM. The SEM fractographs were recorded with an acceleration voltage of 10-15 kV. The microstructure of alloy A (not depicted in the course of this work) consists of elongated grains with an epitaxial growth over several layers towards the building direction. No carbon martensite was formed, as expected from the absence of carbon in the composition. No correlation between crack formation and solidification structure has been observed. In this case cracks propagate linearly over several grains. The SEM fractograph in Figure 14a clearly depicts the presence of transcrystalline fracture surfaces that can be assigned as brittle failure in the solid state (cold cracks).

Regarding the carbon-containing steels, the microstructure consists of needle-like martensite with retained austenite and fine carbidic constituents. It was observed that crack formation can be clearly correlated to the solidification structure, with a further propagation along dendrite boundaries, usually following a “zig-zag” pattern. The presence of dendritic structures on the crack surfaces of all five alloys in Figure 14b-f are suggest the presence of hot cracking as predominant failure mechanism. However, more detailed investigations are necessary in order to determine the influence of varying SEM parameters (i.e. acceleration voltage or different detection modes). The solidified debris of the alloy F produced during the LPBF experimental campaign was also analysed and exhibits the same crack surface structure that can be definitely correlated to the solidification structure.

Figure 15 shows the Vickers microhardness measurements along the build direction of the different processed alloys. Alloys A, B, and C show an increasing hardness trend along the build direction. This can be attributed to the annealing effect of the successive layers on the previous ones as previously observed (Platl et al., (2021) on the same material (alloy B). Similar observations were made by Mertens et al., (2016) concerning AISI H13 tool steel, and by Krakhmalev et al., (2015) concerning with AISI 420 stainless steel. The high micro hardness values obtained at the last layers (top of the samples) are associated with the martensite formation in each of the newly solidified layer as a result of a fast quenching treatment. Instead, when moving away from the last layers, the multiple thermal cycles experienced by the material during the process is expected to lead to the annealing effect of the microstructure and thus a hardness decrease trend over the build direction. On the other

hand, within the overall increasing trend, local hardness drops can be observed such as the one seen in alloy B at approximately 2.4 mm height. Such hardness drops can be attributed to local defects such as pores or cracks beneath the testing position. The steep ascent of the hardness profile observed in alloy C can cause a mismatch under the thermal stresses generated along the part. The alloys D and E show smaller variations of microhardness along the build direction. However, it should be noted that sample height is smaller due to the severe cracking, which may have also led to the release of the thermal stresses and a reduction of the overall hardness.

The overall hardness profile should reflect the microstructural formation as well as the defect amount. The alloy A and B have been proven to be most processable. The increased hardness of B is related to its carbon content. The alloy C has a higher amount of carbon, possible cause for a higher microhardness but also a higher amount of cracks. Resultantly the average hardness is lower than that of alloy B. In the case of alloys E and F, the observed values are limited to the specimens before the failure of the build job, which shows the properties of a material with high amount of defects. Without the presence of such a high degree of cracking, the alloys D and E could have otherwise show much higher hardness.

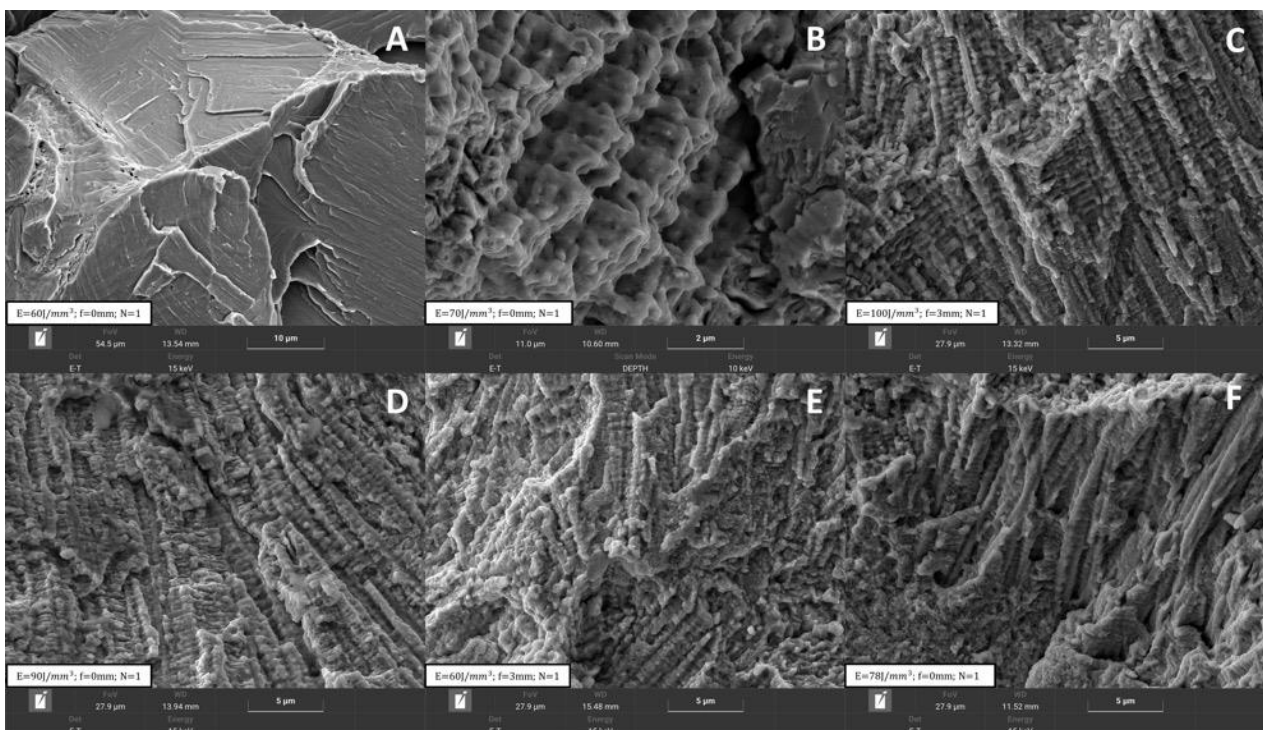


Figure 14: Crack surface fractographs for the six investigated alloys. Images are taken in the scan plane. Letters denote the alloy type. Note the different scale bars and varying process parameters.

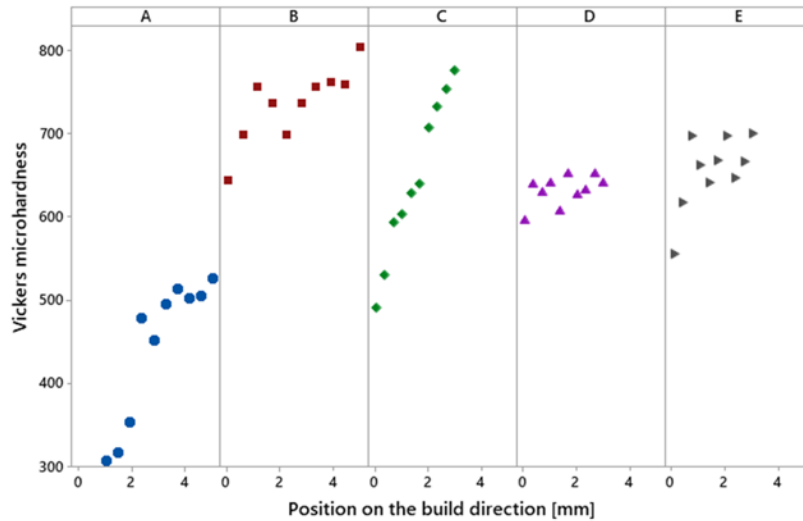


Figure 15: Vickers microhardness measurements along the build direction.

If the structures on the crack surfaces of alloys B-F formed during solidification and are hence freely solidified dendrites, this would also be a clear indication of hot cracking as predominant cracking mechanism. However, if these dendrites are regarded as superstructures, it is also possible that these solidification structures fail in the solid state due to stress accumulations. Hot cracking as predominant crack formation mechanism would be supported by the high  $\Delta T$  estimated with ThermoCalc software. The carbon segregation during solidification and the high CR typical of the LPBF process, push the solidification far from the equilibrium. However, as observed in Figure 13, even if only indicative trends can be assumed, high  $\Delta t_{8/5}$  are desirable for crack mitigation (or equivalently low CR) for alloys C, D, and E. This may imply that the mechanism of crack formation and propagation are different. It can be assumed that hot cracks are firstly formed during solidification. The fast cooling (low  $\Delta t_{8/5}$  and high CR) and the high carbon content foster the martensitic solid-state transformation, which leads to high residual stresses. Hence, cracks propagate especially from the borders towards the internal part of the specimens in an embrittled martensitic dominated microstructure (cold crack propagation). The high CEN endorses the crack propagation mechanism previously described. In particular, alloy B is the least cracked alloy, despite its high  $\Delta T$  (the highest among the tool steels under investigation). The lower cracking tendency may be due to the lower carbon content, which makes this alloy less susceptible to segregation, and thus, to hot cracking. Oppositely, the high carbon content of alloy F induces a stronger segregation susceptibility, especially with rapid cooling, drastically decreasing its processability. Concerning the microstructure, the analysis revealed the presence of a martensite, which, on the contrary, is supposed to be suppressed according to the  $M_s$  indicator. This demonstrates that the indicator  $M_s$  cannot be applied to LPBF

rapid solidification. As the cracking mechanism of carbon-containing tool steels was not the main focus of this work, further investigations that will be published in the course of future research activities are mandatory with regard to this particular crack mechanism.

Regarding alloy A, a different cracking mechanism might explain the failure of this alloy. The carbon absence in the composition strongly influences the analysis as CEN and  $M_s$  indicators cannot be assessed.  $\Delta T$  is significantly lower than for the other steels (approximately 120 K) because the micro segregation of carbon is absent. Moreover, the shown fractographs revealed that crack formation cannot be correlated to the solidification structure. Instead, brittle transcrystalline fracture surfaces are observed together with a linear crack propagation over several grains. The indications from  $\Delta t_{8/5}$  and CR in Figure 13 suggest that faster cooling rates are desirable for crack mitigation. According to the microstructure analysis there could be three contributing factors to the alloy A failure:

- i) Excessive thermal residual stresses developed as a consequence of rapid cooling.
- ii) A combination of high ductile-to-brittle transition temperature with high residual stresses, as suggested in the work of Vrancken et al., (2020), dealing with laser induced microcracking with pure tungsten. When this temperature is reached, dislocations, which are responsible for the plastic deformations, immediately turn immobile. Thus, cracks are triggered when thermal residual stresses exceed the limit of the material.
- iii) Possible formations of ordered domains with null ductility.

## **5 Conclusions**

In the present work, a framework for mapping the LPBF process feasibility of novel high-alloyed tool steels was presented. Cracking was found to be the main defect type, while a good degree of densification could be achieved. LPBF processability drastically decreases with increasing carbon content. In fact, for higher carbon contents, poor consolidation, high distortion, delamination and higher crack densities are observed, even at a macroscopic scale, suggesting that chemical composition plays a key role in the LPBF processability and is more relevant than the contribution from the process parameters. Fractography revealed that crack surfaces of carbon-containing tool steels show dendritic superstructures that can be clearly correlated to the solidification

structure, whilst the carbon-free steel fails in a brittle way, which is obvious due to the presence of transcrystalline structures on the crack surface.

The combination of the explorative tools provided interesting insights about cracking prediction of the carbon-containing tool steels, while their effectiveness is increased when employed in a complementary way. Wide solidification intervals  $\Delta T$ , encouraged by high cooling rates CR and segregation, would suggest a high hot cracking susceptibility. On the other hand, low cooling times  $\Delta t_{8/5}$  and high equivalent carbon contents CEN indicate the likely formation of brittle phases and residual stress development during cooling. This in turn leads to enhanced cold cracking susceptibility.

The occurrence of one cracking mechanism does not exclude the other one. Cracks could be triggered during solidification but then propagate easily in a brittle microstructure. This eventually implies that none of the indicator works independently for defect prediction. Instead, the mapping effectiveness is based on the combined use of the tools.

Concerning the  $M_s$  temperature tool, a strong contradiction was found. For any of the carbon-containing steels, martensite is predicted to be suppressed when, instead, it was observed in the microstructure. This demonstrates that commonly used  $M_s$  temperature formulas are not directly applicable to LPBF processed materials.

Within this work, the empirical and physical tools were exploited principally for a phenomenological comprehension of the defect formation mechanisms leading to scarce processability. The results show that the indicators employed with designed experiments are highly effective in evaluating the processability and defect formation mechanisms. The use of a single parameter fails to describe the processability of the highly complex chemical compositions employed.

An important outcome of the work is related to the fact that the conventional LPBF machine architectures may not be sufficient to mitigate the defects through the manipulation of the energy input in space and time. With the aid of more advanced datamining and artificial intelligence means, the approach can be exploited in a more automated way towards designing new alloys.

## **Acknowledgements**

The Italian Ministry of Education, University and Research is acknowledged for the support provided through the Project “Department of Excellence LIS4.0 - Lightweight and Smart Structures for Industry 4.0”. In addition, funding from the Austrian BMK (846933) in the framework of the program “Production of the future” and the “BMK Professorship for Industry” is gratefully acknowledged.



## 6 Appendix

### 6.1 Cooling rate and cooling time

Cooling rates CR and cooling times  $\Delta t_{8/5}$  are usually exploited in welding operations to foresee the severity of cooling and the grain size, thus providing insights about microstructure evolution during solidification. Cooling rate describes how fast the cooling process is, whereas cooling time is the estimation of cooling time between 800°C and 500°C. High cooling rates and low cooling times usually lead to non-equilibrium transformations, which result in brittle solid phases such as martensite in carbon steels and high residual stresses after cooling.

The formulations of cooling rate and time are derived from the famous Rosenthal equations for a moving heat source. However, lots of strict assumptions are needed to obtain the analytical expressions such as homogeneity of the material, absence of mass movement, no phase changes, no heat source inside the volume, constant travel speed of the heat source, the shape of the heat source (point or linear) and the point of validity (centre of the weld).

Zhang et al., (2019) stated that heat source modelling is an important task since the heat source shape directly influences the melt pool geometry and the mechanical performance of final products. The heat source shape can be distinguished between 2D (linear) or 3D (point). To simulate the LPBF process, Zhang et al., (2019), Yadroitsev et al., (2009) and Liu et al., (2018) agree that it may be improper to adopt two dimensional heat sources because the scanning layer over metal powder can penetrate into the powder bed. In fact, two-dimensional heat sources assume energy deposition on the top surface of the powder bed and not inside. Therefore, in the present investigation, it was decided to choose a three-dimensional heat source.

Starting from these assumptions, Ouden and Hermans, (2009) state that it is possible to derive the following expressions to estimate the cooling rate and the cooling time:

$$CR \left( \frac{K}{s} \right) = - \frac{2\pi k(T-T_0)^2}{W}, \quad 3$$

$$\Delta t_{85} (s) = \frac{W}{2\pi k} \left\{ \frac{1}{500-T_0} - \frac{1}{800-T_0} \right\}, \quad 4$$

where  $k$  is the coefficient of thermal conductivity,  $T_0$  is the preheating temperature and  $W$  is the heat input, which is expressed in J/m. Note that the starting point for the estimation of cooling rates and cooling times are not derived under the assumption of a heat source (laser source in this work) that operates in a pulsed regime by power modulation, like the LPBF industrial machine used in this work. According to this operating regime, some of the parameters appearing in the previous equation must be adapted. In Table 7 the adapted parameters to the LPBF process and their formulas are provided.

Table 7: Adapted parameters to LPBF machine operating in a pulsed regime.

Symbol	Meaning
$v = pd^{(1)}/t_{on}^{(2)}$	travel speed
$W = P/v$	heat input
(1) pd is the point distance	
(2) ton is the pulse duration	

## 6.2 Equivalent carbon content

Wang, (2015) defines the equivalent carbon content as an empirical indicator typically used in welding to foresee the weldability of an alloy, in particular to predict the heat affected zone hardenability and its tendency to form cold cracks. In the literature, there exist many formulas for the calculation of this indicator. However, each of them suffer from strict validity ranges, usually given in terms of the alloy chemical composition or carbon content.

In this work it was decided to use the formulation proposed by Yurioka et al. (Yurioka, (2001); Yurioka et al., (1983)):

$$CEN = C + A(C) * \left( \frac{Si}{24} + \frac{Mn}{6} + \frac{Cu}{15} + \frac{Ni}{60} + \frac{Cr+Mo+Nb+V}{5} + 5B \right) (wt. \%), \quad 5$$

with

$$A(C) = 0.75 + 0.25 * \tanh(20 * (C - 0.12)). \quad 6$$

The reason of this choice is that this indicator has been developed based on a wide variety of steels, ranging from low carbon steels to high carbon steels, so it is more appropriate to deal with the special steels under investigation (tool steels) featured by high carbon content. Although it was developed for determined ranges of steels, it is very simple to calculate since it is only composition – dependent. In the present work it is used as a cold cracking indicator.

### 6.3 Martensite start temperature

The temperature of martensite start corresponds to the temperature at which the martensitic solid-state transformation takes place. Usually, martensite is formed in carbon steels due to sufficiently rapid cooling (e.g. also used in quenching heat treatments)) of the face-centered cubic austenite. An excessive cooling rate guarantees that the carbon atoms cannot be incorporated along the c axis of the tetragonally distorted body-centered martensite. The latter is highly supersaturated in carbon and other alloying elements after the transformation. If cooling rates are too low to guarantee this martensitic transformation, other microstructure constituents (e.g. perlite, bainite, etc.) can be formed.

As stated in the work of Peet et al. (Peet, 2015), in the literature many authors exploit linear regression equations completely based on the chemical composition of the alloy to calculate the  $M_s$ . Usually they take the form of:

$$M_s = k_0 + \sum k_i w_i \text{ (wt. \%)}, \quad 7$$

where  $k_0$  is the  $M_s$  of the pure iron,  $w_i$  is the concentration of the  $i$ -th alloying element usually expressed in weight percentage while  $k_i$  is a coefficient that relates the concentration of the  $i$ -th alloying element with a  $M_s$  variation. Such equations have the advantage of giving a very fast approximation of this parameter but they are usually limited to specific range of compositions, and the boundaries of this range are often vague or not determined. Moreover, like in this work, there is often a temptation to use these regression models outside the range of composition where they have been derived: it is worth to underline that the values obtained applying these models for alloys outside the range composition are just indicative of the order of magnitude and the behaviour when the carbon content is varied. The reason is that even with binary alloys, there exists a non-linear dependence on solute concentration, moreover  $M_s$  depends also on the thermodynamics of the process. In the present work the following formulas for the  $M_s$  estimation were used:

$$M_{s0}(K) = 561 - 474 * C - 33 * Mn - 17 * Cr - 17 * Ni - 21 * Mo - 7.5 * Si \text{ (wt. \%)} + 273.15, \quad 8$$

$$M_{s1}(K) = 550 - 350 * C - 40 * Mn - 35 * V - 20 * Cr - 17 * Ni - 10 * Cu - 10 * Mo - 8 * W + 273.15, \quad 9$$

$$M_{s2}(K) = 0.495 * M_{s1} + 0.00095 * M_{s1} + 313.15 \quad 10$$

As reported in the work of Platl et al., (2020b), these empirical equations can be used to estimate the martensite start temperature of alloyed steel at different austenitizing temperatures. Although their simple formulation, being based only on the chemical composition of the alloy, in the present work they are used as a martensite suppression indicator.

#### **6.4 Estimation of the solidification interval**

The solidification of alloys does not occur at one specific temperature but takes place in a range of temperatures known as solidification interval. The knowledge of this parameter is of paramount importance because it is in this range of temperatures that solidification cracks may develop and the broader this interval is, the higher is the risk of cracking. However, it is not easy to have its estimate being dependent mostly on thermodynamics of the process and the chemical composition of the material. It was decided to rely on simulations implemented in Thermocalc software to estimate this indicator.

Thermocalc software allows the calculation of the solidification intervals by means of simulations based on the Scheil-Gulliver (SG) model. Kozeschnik et al., (2007) and Schaffnit et al., (2015) state that this model is based on three basic assumptions:

- Negligible diffusion of elements in the solid phase.
- Infinitely fast diffusion in the liquid phase.
- Local thermodynamic equilibrium is established at the solid/liquid interface during solidification.

According to Kozeschnik et al., (2007), when running a classical SG-model, the simulation starts in the liquid phase (first step). Following an iterative procedure, the temperature is decreased stepwise of a certain small quantity which can be specified during setting before the simulation starts (second step). In each iteration-step, thermodynamic equilibrium is calculated between the liquid and the solid phases (third step). At the point at which solid phases become thermodynamically stable due to the liquid undercooling, they can appear in amounts according to thermodynamic equilibrium between the liquid and the newly formed phases (local equilibrium hypothesis). In all the other iteration steps, these solid phases remain unaltered both in amount and chemical composition (fourth step). Therefore, the chemical composition of the remaining liquid changes according to the mass conservation principle (fifth step). Then, the second to the fifth steps are repeated until all the liquid is transformed into solid.

However, when this model is adopted, very broad solidification intervals can be returned, which can be very different from experimental measures of the same intervals. Kozeschnik et al., (2007) states that this is due to the strong segregation of carbon in the model, which actually may not occur. In fact, the situation changes significantly if interstitial elements like carbon or nitrogen are involved: their diffusion during solidification is usually too fast to justify the assumption of the SG model of negligible diffusion in the solid. What happens in reality is that although interstitial elements are rejected into the liquid initially, their fast diffusion allows their redistribution back into the solid. This process is known as back-diffusion.

The commercially available Thermocalc software is equipped with the back-diffusion modality which can return more accurate results. When this modality is enabled, the previous algorithm of the classical SG simulation is modified. In fact, after the previously described steps, an additional computational step is performed to mimic the partial redistribution of fast diffusers between the liquid and the solid phases. This is performed by constraining the thermodynamic equilibrium “compositionally”, which means that substitutional element contents of each phase and the amount of these phases are frozen while fast diffusers (interstitial elements) are allowed to redistribute.

In Thermocalc chemical compositions of the alloys were set using the available databases TCFE9 (Steels/Fe-Alloys v9.1) and MOBFE4 (Steels/Fe-Alloys Mobility v4.0). Concerning the simulation, the following parameters have been set equal for all the alloy grades for a direct comparison under the same solidification conditions:

- Cooling rate:  $10^4$  K/s
- Terminate on fraction of liquid phase at 0.05%

Concerning the cooling rate, typical values of the LPBF cooling rates are used as suggested from Saewe et al., (2019) and J. Sander et al., (2017). The simulations were all ended at a fraction of liquid phase at 0.05% as described before. Thermocalc allows the simulation to terminate at even lower thresholds, however as suggested from (Kozeschnik et al., 2007), 0.05% is a usual cut-off value pragmatically selected because of its agreement with experimental data. Choosing lower threshold physically means that simulation is concluded when the last atom of liquid is solidified, thus enlarging even more the solidification intervals, however due to the agreement with the experimental data, even if remaining liquid is left, the solidification is assumed to be

concluded. A calibration for the simulation has been run before the experimental activity with stainless steel AISI316L.

## 6.5 Volumetric energy density

Volumetric energy density is the energy transmitted by the laser beam per unit volume. It is calculated according to Equation 11 proposed by Carluccio et al., (2019), considering the pulsed wave mode of the LPBF machine exploited throughout this work.

$$E \left( \frac{\text{J}}{\text{mm}^3} \right) = \frac{P t_{\text{on}}}{p_d h_d z} \quad 11$$

where  $P$  is the laser power,  $t_{\text{on}}$  is the pulse duration,  $p_d$  is the point distance,  $h_d$  is the hatch distance and  $z$  is the layer thickness. According to Saewe et al., (2020), this parameter can be used to compare the theoretical energy input of the laser beam into the material for different process parameters.

## References

- Beal, V.E., Erasenthiran, P., Hopkinson, N., Dickens, P., Ahrens, C.H., Erasenthiran, P., Hopkinson, N., Dickens, P., Ahrens, C.H., 2008. Scanning strategies and spacing effect on laser fusion of H13 tool steel powder using high power Nd : YAG pulsed laser 7543. doi:10.1080/00207540500168279
- Buls, S., Humbeeck, J. Van, 2014. Selective Laser Melting of Crack-Free High Density M2 High Speed Steel Parts by Baseplate Preheating 136, 1–6. doi:10.1115/1.4028513
- Carluccio, D., Demir, A.G., Caprio, L., Previtali, B., Bermingham, M.J., Dargusch, M.S., 2019. The influence of laser processing parameters on the densification and surface morphology of pure Fe and Fe-35Mn scaffolds produced by selective laser melting. J. Manuf. Process. 40, 113–121. doi:10.1016/j.jmapro.2019.03.018*
- Cunningham, R., Narra, S.P., Rollett, A.D., 2017. Synchrotron-Based X-ray Microtomography Characterization of the Effect of Processing Variables on Porosity Formation in Laser Power-Bed Additive Manufacturing of Ti-6Al-4V Synchrotron-Based X-Ray Microtomography Characterization of the Effect of Processin. doi:10.1007/s11837-016-2234-1
- Danninger, H., Siman, F., Iždinský, K., 2013. Powder metallurgy carbon free tool steels Fe-Co-Mo with varying Co and Mo contents 13, 47–56.
- Demir, A.G., De Giorgi, C., Previtali, B., 2017. Design and implementation of a multi-sensor coaxial monitoring system with correction strategies for selective laser melting of a maraging steel. J. Manuf. Sci. Eng. 140, 1–14. doi:10.1115/1.4038568*
- Demir, A.G., Previtali, B., 2017. Investigation of remelting and preheating in SLM of 18Ni300 maraging steel as corrective and preventive measures for porosity reduction. Int. J. Adv. Manuf. Technol. 93. doi:10.1007/s00170-017-0697-z*
- Fayazfar, H., Salarian, M., Rogalsky, A., Sarker, D., Russo, P., Paserin, V., Toyserkani, E., 2018. A critical review of powder-based additive manufacturing of ferrous alloys: Process parameters, microstructure and mechanical properties. Mater. Des. 144, 98–128. doi:10.1016/j.matdes.2018.02.018
- Kouraytem, N., Li, X., Tan, W., Kappes, B., Spear, A., 2020. Modeling process-structure-property

relationships in metal additive manufacturing: a review on physics-driven versus data-driven approaches.

J. Phys. Mater. doi:10.1088/2515-7639/abca7b

Kozeschnik, E., Rindler, W., Buchmayr, B., 2007. Scheil Gulliver simulation with partial redistribution of fast diffusers and simultaneous solid - solid phase transformations. *Int. J. Mater. Res.* 98, 826–831.

Krakhmalev, P., Yadroitsava, I., Fredriksson, G., Yadroitsev, I., 2015. In situ heat treatment in selective laser melted martensitic AISI 420 stainless steels. *Mater. Des.* 87, 380–385. doi:10.1016/j.matdes.2015.08.045

Krell, J., Röttger, A., Geenen, K., Theisen, W., 2018. General investigations on processing tool steel X40CrMoV5-1 with selective laser melting. *J. Mater. Process. Tech.* 255, 679–688. doi:10.1016/j.jmatprotec.2018.01.012

Liu, S., Zhu, H., Peng, G., Yin, J., Zeng, X., 2018. Microstructure prediction of selective laser melting AlSi10Mg using finite element analysis. *Mater. Des.* 142, 319–328. doi:10.1016/j.matdes.2018.01.022

Liu, Z.H., Chua, C.K., Leong, K.F., Kempen, K., Thijs, L., Yasa, E., Kruth, J.P., 2011. A Preliminary Investigation on Selective Laser Melting of M2 High Speed Steel.

Martin, A.A., Calta, N.P., Khairallah, S.A., Wang, J., 2019. Dynamics of pore formation during laser powder bed fusion additive manufacturing. *Nat. Commun.* 1–10. doi:10.1038/s41467-019-10009-2

Mertens, R., Vrancken, B., Holmstock, N., Kinds, Y., Kruth, J.P., Van Humbeeck, J., 2016. Influence of powder bed preheating on microstructure and mechanical properties of H13 tool steel SLM parts. *Phys. Procedia* 83, 882–890. doi:10.1016/j.phpro.2016.08.092

Narvan, M., Al-rubaie, K.S., Elbestawi, M., 2019. Process-Structure-Property Relationships of AISI H13 Tool Steel Processed with Selective Laser Melting 1–20.

Ouden, G. den, Hermans, M.J.M., 2009. *Welding Technology*, First. ed. VSSD, Delft.

Peet, M., 2015. Prediction of martensite start temperature. *Mater. Sci. Technol. (United Kingdom)* 31, 1370–1375. doi:10.1179/1743284714Y.00000000714

Platl, J., Leitner, H., Turk, C., Demir, A.G., Previtali, B., Schnitzer, R., 2020a. *Defects in a Laser Powder Bed Fused Tool Steel.* doi:10.1002/adem.202000833



- Platl, J., Leitner, H., Turk, C., Schnitzer, R., 2020b. Determination of Martensite Start Temperature of High-Speed Steels Based on Thermodynamic Calculations. *Steel Res. Int.* 91, 1–8. doi:10.1002/srin.202000063
- Platl, J., Rainer, D., Galbusera, F., Leitner, H., Turk, C., Demir, A.G., Previtali, B., Schnitzer, R., 2021. Potential Causes for Cracking of a Laser Powder Bed Fused Carbon-free FeCoMo alloy, in: *Proceedings of the Metal Additive Manufacturing Conference (MAMC)*. Vienna, Austria.
- Poorhaydari, K., Patchett, B.M., Ivey, D.G., 2005. Estimation of Cooling Rate in the Welding of. *Weld. J.* 149–155.
- Saewe, J., Gayer, C., Jauer, L., Kunz, J., Broeckmann, C., Schleifenbaum, J.H., 2020. Feasibility investigation for laser powder bed fusion of high-speed steels. *Euro PM 2018 Congr. Exhib.* 3–10.
- Saewe, J., Gayer, C., Kunz, J., Broeckmann, C., Schleifenbaum, J.H., 2018. Influence of Powder Bed Temperature on Microstructure and Post Heat Treatment of HSS AISI M50 Processed by LPBF.
- Saewe, J., Gayer, C., Vogelpoth, A., Schleifenbaum, J.H., 2019. Feasability Investigation for Laser Powder Bed Fusion of High-Speed Steel AISI M50 with Base Preheating System. *BHM Berg- und Hüttenmännische Monatshefte* 164, 101–107. doi:10.1007/s00501-019-0828-y
- Sander, J., Hufenbach, J., Bleckmann, M., Giebeler, L., Wendrock, H., Oswald, S., 2017. Selective laser melting of ultra-high-strength TRIP steel : processing , microstructure , and properties 4944–4956. doi:10.1007/s10853-016-0731-9
- Sander, J., Hufenbach, J., Giebeler, L., Bleckmann, M., Eckert, J., Kühn, U., 2017. Microstructure, mechanical behavior, and wear properties of FeCrMoVC steel prepared by selective laser melting and casting. *Scr. Mater.* 126, 41–44. doi:10.1016/j.scriptamat.2016.07.029
- Sander, J., Hufenbach, J., Giebeler, L., Wendrock, H., Kühn, U., Eckert, J., 2016. Microstructure and properties of FeCrMoVC tool steel produced by selective laser melting. *Mater. Des.* 89, 335–341. doi:10.1016/j.matdes.2015.09.148
- Schaffnit, P., Stallybrass, C., Konrad, J., Stein, F., Weinberg, M., 2015. A Scheil-Gulliver model dedicated to the solidification of steel. *Calphad Comput. Coupling Phase Diagrams Thermochem.* 48, 184–188.

doi:10.1016/j.calphad.2015.01.002

- Smith, J., Xiong, W., Yan, W., Lin, S., Cheng, P., Kafka, O.L., Wagner, G.J., Cao, J., Liu, W.K., 2016. Linking process, structure, property, and performance for metal-based additive manufacturing: computational approaches with experimental support. *Comput. Mech.* 57, 583–610. doi:10.1007/s00466-015-1240-4
- Spierings, A.B., Schneider, M., Eggenberger, R., 2011. Comparison of density measurement techniques for additive manufactured metallic parts. *Rapid Prototyp. J.* 17, 380–386. doi:10.1108/13552541111156504
- Thermocalc, 2021. TCFE9-Steels/Fe-Alloys v9.1 and MOBFE4-Steels/Fe-Alloys Mobility v4.0.
- Vrancken, B., Ganeriwala, R.K., Matthews, M.J., 2020. Analysis of laser - induced microcracking in tungsten under additive manufacturing conditions : experiment and simulation. *Acta Mater.* doi:10.1016/j.actamat.2020.04.060
- Wang, W., 2015. The Great Minds of Carbon Equivalent Part III : The Evolution of Carbon Equivalent Equations Material G, 9–11.
- Wu, L., Das, S., Gridin, W., Leuders, S., Kahlert, M., Vollmer, M., Niendorf, T., 2021. Hot Work Tool Steel Processed by Laser Powder Bed Fusion: A Review on Most Relevant Influencing Factors. *Adv. Eng. Mater.* 2100049. doi:10.1002/adem.202100049
- Yadroitsev, I., Bertrand, P., Smurov, I., 2009. Model of Radiation and Heat Transfer in Laser-Powder Laser Melting 131, 1–10. doi:10.1115/1.3109245
- Yan, J.J., Zheng, D.L., Li, H.X., 2017. Selective laser melting of H13 : microstructure and residual stress 12476–12485. doi:10.1007/s10853-017-1380-3
- Yan, W., Lin, S., Kafka, O.L., Yu, C., Liu, Z., Lian, Y., Wolff, S., Cao, J., Wagner, G.J., Liu, W.K., 2018. Modeling process-structure-property relationships for additive manufacturing. *Front. Mech. Eng.* 13, 482–492. doi:10.1007/s11465-018-0505-y
- Yurioka, N., 2001. Physical metallurgy of steel weldability. *ISIJ Int.* 41, 566–570. doi:10.2355/isijinternational.41.566
- Yurioka, N., Suzuki, H., Ohshita, S., Saito, S., 1983. Determination of Necessary Preheating Temperature in

Steel Welding. Weld. J. (Miami, Fla) 62.

Zhang, Z., Huang, Y., Kasinathan, A.R., Shahabad, S.I., Ali, U., 2019. 3-Dimensional heat transfer modeling for laser powder-bed fusion additive manufacturing with volumetric heat sources based on varied thermal conductivity and absorptivity. Opt. Laser Technol. 109, 297–312. doi:10.1016/j.optlastec.2018.08.012

Zou, J., Gaber, Y., Voulazeris, G., Li, S., Vazquez, L., Liu, L., Yao, M., Wang, Y., Holynski, M., Bongs, K., Attallah, M.M., 2018. Acta Materialia Controlling the grain orientation during laser powder bed fusion to tailor the magnetic characteristics in a Ni-Fe based soft magnet 158, 230–238. doi:10.1016/j.actamat.2018.07.064

## List of tables

Table 1: Chemical compositions of tool steels reported in the literature. Each content in the composition is expressed in wt.%.....	4
Table 2: List of analytical and empirical models used in this work.....	9
Table 3: Designation and nominal chemical compositions of the tool steels alloys. Letters denote the alloy type.....	11
Table 4: Thermophysical properties of the alloys under investigation at room temperature declared by the powder provider. ....	11
Table 5: Fixed and varied parameters used in the experimental campaign .....	12
Table 6: Analysis of variance on crack density and model summary .....	19
Table 7: Adapted parameters to LPBF machine operating in a pulsed regime.....	33

## List of figures

Figure 1: SEM images showing the spherical morphology of the used powders. Letters denote the alloy type. ....	11
Figure 2: a) Metallographic cross section; b) Black and white conversion of the cross section. ....	13
Figure 3: Detail of crack extension measurements. Yellow segments denote the crack route and red circles denote pores.....	14
Figure 4: Top and back view of the building platforms for each alloy. Letters denote the alloy type. ....	15
Figure 5: Metallographic cross sections comparison between the worst and best cases in terms of relative density for each alloy. “BD” stands for Build Direction while letters denote the alloy type.....	16
Figure 6: Relative density in dependence of the process parameters for each processed alloy.....	16
Figure 7: Metallographic cross sections comparison between the worst and best cases in terms of crack density for each alloy. “BD” stands for Build Direction while letters denote the alloy type. ....	17

Figure 8: Crack density as a function of the process parameters for each processed alloy. ....	18
Figure 9: a) Main effects plot of CD data; b) Interaction plot of CD data. ....	19
Figure 10: Solidification simulations expressed in T (K) vs Mole fraction of solid diagrams, for all six investigated alloys. Dotted, red and blue lines denote the solidification simulation according to the equilibrium model (EQ), Scheil Gulliver model (SG) and Scheil Gulliver model with back diffusion of carbon (SGS-BF). ....	21
Figure 11: Thermocalc estimations of solidification intervals according to equilibrium solidification model (EQ) and Scheil Gulliver model with back diffusion (SGS-BF). ....	22
Figure 12: Crack density as a function of a) carbon equivalent content; b) martensite start temperature; and c) solidification interval. ....	24
Figure 13: Crack density as a function of a) cooling time and b) cooling rate for the processed alloys. Dashed lines only indicate trends. ....	25
Figure 14: Crack surface fractographs for the six investigated alloys. Images are taken in the scan plane. Letters denote the alloy type. Note the different scale bars and varying process parameters. ....	27
Figure 15: Vickers microhardness measurements as a along the build direction. ....	28